WAVES IN RANDOM AND COMPLEX MEDIA

https://www.tandfonline.com/journals/twrm20

Impact factor = 4.853

ACCEPTED DECEMBER 6TH 2022

LATTICE BOLTZMANN SIMULATION OF THERMO-MAGNETIC NATURAL CONVECTION IN AN ENCLOSURE PARTIALLY FILLED WITH A POROUS MEDIUM

***K. Venkatadri*[1*] and *O. Anwar Bég*[2]**

[1]*Department of Mathematics, Indian Institute of Information Technology Sri City, Chittoor-517464,* ***A.P., India.***

[2]*Multi-Physical Engineering Sciences Group, Aeronautical/Mechanical Engineering, Salford University, School of Science, Engineering and Environment (SEE), Manchester, M54WT,* ***UK***

**Corresponding author- email: venkatadri.venki@gmail.com, venkatadri.k@iiits.in*

ABSTRACT

Motivated by emerging magnetized hybrid fuel cell applications, a theoretical analysis of incompressible magnetohydrodynamic (MHD) non-Darcian thermogravitational convection in a square enclosure partially filled with a highly permeable medium in presence of transverse magnetic field is presented. The enclosure is filled with magnetized Newtonian fluid. A non-Darcy model is utilized for the porous region featuring both Darcian linear drag and second order Forchheimer drag components with Brinkman no-slip at the walls. The horizontal (i.e., bottom and Top) wall boundaries are considered adibatic and impermeable, while the side walls (hot and cold walls) are maintained with different thermal values. The Lattice Boltzmann method (LBM) is implemented to employ the governing momenta and thermal conservation equations with appropriate end conditions. The divergence of the non-linear system is avoided by introducing convergence criteria factors. A grid independence test is included for validation of the D2Q9-LBM code accuracy. Further validation with earlier studies in the absence of Hartmann number (Ha) is included. A parametric examination of the impact of Hartmann number ($0 < Ha < 50$), Darcy number ($0.0001 < Da < 0.1$), and Rayleigh number ($10^3 < Ra < 10^6$) on temperature contours and streamline patterns for Helium gas (Prandtl number (Pr) = 0.71) is conducted. The heat flux distributions on the side walls and centre-line velocity are also computed. With greater Darcy number and Rayleigh number, Nusselt number is boosted at the left hot wall and the right cold wall. However, Nusselt number increases as one descends

the hot wall towards the lower adiabatic boundary whereas for it increases as one ascends the cold wall towards the upper adiabatic boundary.

KEYWORDS: *D2Q9 lattice model; Darcy-Forchheimer-Brinkman model; Enclosure; Hartmann number; Hybrid fuel cells; Lattice Boltzmann method (LBM); Magneto-convection; Partial porous medium; Thermal buoyancy.*

NOMENCLATURE

B_0	Magnetic field, Tesla
c	Lattice velocity, m s^{-1}
c_s	Speed of the sound, m s^{-1}
c_i	Discrete particle speed, m s^{-1}
C_p	Specific heat at constant pressure, J K^{-1} kg^{-1}
Da	Darcy number (-)
F_i	External forces, N
f	Density distribution functions, kg m^{-3}
f^{eq}	Equilibrium density distribution functions, kg m^{-3}
g	Internal energy distribution functions, K
Ha	Hartmann number (-)
g^{eq}	Equilibrium internal energy distribution functions, K
g	Gravitational acceleration, m s^{-2}
k	Thermal conductivity, W K^{-1} m^{-1}
L	Length and height of the enclosure, m
m	Number of lattices in *y* direction
Nu	Local Nusselt number (-)
n	Number of lattices in *x* direction
P	Pressure, N m^{-2}
Pr	Prandtl number (-)
Ra	Rayleigh number (-)
T	Temperature, K
$\mathbf{u}(u,v)$	Velocities, m s^{-1}

$\mathbf{x}(x, y)$	Lattice coordinates, m

Greek symbols

α	Thermal diffusivity, $m^2 s^{-1}$
β	Thermal expansion coefficient, K^{-1}
θ	Non-dimensional temperature
μ	Dynamic viscosity, kg $m^{-1} s^{-1}$
ν	Kinematic viscosity, $m^2 s^{-1}$
ρ	Density, kg m^{-3}
σ	Electrical conductivity, S m^{-1}
ϕ	Solid volume fraction
τ_α	Relaxation time for flow, s
τ_v	Relaxation time for temperature, s
Δx	Lattice spacing, m
Δt	Time increment, s
ψ	Non-dimensional stream function
w_i	Weighting factor for flow
w_i'	Weighting factor for temperature
Δ	Difference

1. INTRODUCTION

Global trends for sustainable and renewable energy resources have stimulated considerable interest in smart energy systems. Many new fuel cells are now being explored which exploit

electromagnetic fluids and allow greater control and enhanced long-term performance. Among the many technologies being developed, magnetic fuel cell systems in which ionized gases are deployed such as hydrogen and helium have received considerable attention in a range of applications including magnetic refrigeration [1] and automotive systems [2, 3]. Magneto-tomography [4] has also emerged as a useful non-invasive technique for assessing fuel cell efficiency and involves a quantification of magnetic flux around the fuel stack generated by electrical current within the stack. Magnetic field has been shown experimentally to favourably influence the efficiency of proton exchange membrane (PEM) fuel cells achieving higher electricity production even at relatively low magnetic field strengths of 16 to 26 microTesla, as described by Abdel-Rehim [5]. Other excellent studies of PEM and other magnetic fuel cells such as microbial magnetic fuel cells include Lin et al. [6], Matsushima et al. [7], Okada et al. [8], Tao and Zhou [9], Ruksawong et al. [10] and Szczes et al. [11]. Many of these studies have confirmed that magnetic field impacts beneficially the diffusion process of the oxygen molecules in fuel cells which leads to improved performance.

Another popular hybrid fuel cell that has been studied in recent years exploits the use of porous materials. Porous media such as cellular foams and porous metals offer a number of advantages including controllable structure, enhanced surface area, flow distribution control and improved distribution of ionized gases to achieve enhanced power density and superior electrochemical performances in fuel cells [12]. Several investigations have been perform using porous media in fuel cell enclosures including Wang [13], Carton and Olabi [14], Lefebvre et al. [15], Tan et al. [16] and Senn and Poulikakos [17]. These investigations generally considered the porous medium to obey Darcy's law, which is valid for viscous-dominated flows with low Re values. However, at higher operational velocities, inertial effects become significant in porous media transport and non-Darcy models are required [18], of which the Darcy-Forchheimer model is quite popular. This uses a supplementary second order drag force to characterize the behaviour at higher Reynolds numbers.

In recent years engineers have explored the combination of both magnetic fluids and porous media in fuel cell systems. To optimize the design of these hybrid electromagnetic porous media fuel cells, in addition to experimentation, mathematical and numerical simulation provides an excellent platform. These hybrid fuel cells feature multi-physical viscous transport in enclosures and to robustly simulate such systems, magnetohydrodynamic (MHD) [19] viscous flow models with heat transfer, mass transfer and other effects such as porous media are required for robustly analysing the transport phenomena inherent to such systems. A

number of studies have been communicated concerning magneto-convection in porous media enclosure fuel cells systems. Krakov and Nikiforov [20] repots the hydromagnetic convection flow in a cavity with a finite element method. showed that transverse magnetic strength is very effective in regulating heat flux via the porous geomentry and that at high magnetic Rayleigh number there is a considerable boost in heat flux. Ahmed and Raizah [21] deployed a modified Galerkin FEM to simulate the thermomagnetic mixed convection in non-Newtonian hybrid nanofluids in complex driven triangular enclosures containing elliptic obstacles, under an oblique magnetic field. Beg et al. [22] used marker and cell (MAC) finite difference scheme along pressure-velocity coupling to compute the thermogravitational flow induced by Lorenz forces of natural convection in a porous regime containing Helium gas under heat generation influence.

The above studies considered the enclosure to be fully occupied with a porous medium. However, it is possible to design fuel cells which are only partially filled with porous medium and are adjacent to a purely fluid zone. Tong and Subramanian [23] presented an early study of steady-state buoyancy-driven convective flow in an enclosure filled with partial porous layer vertically, delineated by an impermeable wall. Used a modified Darcy's law with Brinkman vorticity diffusion to simulate the porous zone and a finite-difference scheme to compute the transport in the two regions, observing that heat transfer can be successfully controlled by partial deployment of a porous medium. Al-Nimr and Khadrawi [24] used Laplace transform methods and the Brinkman-extended Darcy model to analyse the transient free convection in isothermal-walled domains partly filled with porous substrates. Beckermann et al. [25] reported on computational and experimental studies of natural convection in a non-square enclosure (aspect ratio =2) filled with porous medium partially.

Thus far relatively sparse work has been reported on MHD convection in an enclosure fuel cell geometry with dual porous media and fluid zones. This is the present focused investigation. The LBM numerical technique [26] is deployed, which is a powerful numerical scheme in which of finite difference technique, finite element methods etc. LBM is a mesoscopic computational approach based on particle representation, although averaged macroscopic behaviour is considered. It essentially employs a gas-kinetic approach to simulate fluid systems and the kinetic nature of LBM is characterized by several features which are distinct from other computational techniques. These include the linear nature of the convection operator in the velocity phase and the deployment of a minimum set of velocities in the phase space. Essentially viscous flows can be simulated by constructing simplified, fictitious molecular

dynamics. A popular LBM methodology is the adoption of the single-relaxation-time collision model. LBM has been deployed extensively in past few years and has been utilized to study a wide range of fluid mechanics problems including natural convection enclosure flows for solar greenhouses [27], magneto-convection flow simulation [28], non-Newtonian transport in enclosures for materials processing [29], entropy generation in magnetic heat transfer in porous media micro-ducts [30]. LBM has also been used to study transport in porous media. Relevant studies include Rong et al. [31] who deployed LBM to study flow and heat transfer in variable porosity Darcian permeable media. Chai et al. [32] utilized LBM to study non-Darcy flow in disordered porous media. Hasert et al. [33] have also simulated non-Darcian transport in porous media with LBM. The simulations are relevant to emerging magnetic hybrid fuel cell systems [34], ionic fuel cells [35] and may also have applications in ceramic microbial fuel cells [36], helium fluidized magnetic bed fuel cells [37] and other processes in the energy industry [38]. Hamzah et al. [42] examined conjugate heat-transfer of a rotating cylinder immersed in Fe_3O_4-water nanofluid under the heat-flux and magnetic field. The average Nusselt number increases by increasing the NPs volume fraction, inclination angle and thermal conductivity ratios, while increasing the Hartmann number decreased the Nusselt number. Almensoury et al. [43] investigated the free convective heat transfer of a non-Newtonian nanofluid through an F-shaped porous cavity. the Nusselt number and velocity rates are directly proportional to the AR, Darcy number (*Da*), and Rayleigh number (*Ra*), and negatively proportional to the power-law index (n). Jabbar et al. [44] presented Convective heat transfer in Copper–water nanofluid fills the porous cavity conjugated with an active rotating cylinder. Hashim et al. [45] optimize the thermal insulation of red clay bricks used in the walls of buildings by using a multiscale method. Abdulkadhim et al. [46] examined more complex geometry, magnetohydrodynamic natural convection of nanofluid (Cu-water) in a wavy walled enclosure having a circular hot cylinder inside. Ali et al. [47] examined the impact of an external magnetic field on the hydrothermal aspects of natural convection of a power-law non-Newtonian nanofluid inside a baffled U-shape enclosure. Ali et al. [48] inspected the MHD mixed convection due to a rotating circular solid cylinder in a trapezoidal enclosure filled with a Cu-water nanofluid saturated with a porous media. Ali et al. [49] proposed the heat transfer, fluid flow and heat capacity ratio are analyzed in an annulus enclosure filled with porous and saturated by a suspension of nanoencapsulated phase change materials (NEPCMs). Hussein et al. [50] studied the laminar two-dimensional mixed convection in a trapezoidal enclosure with a rotating inner circular cylinder and a sinusoidal bottom wall, fluid inside the enclosure is a CuO–water nanofluid layer in the top space of it, while the bottom space includes a CuO–water nanofluid

saturated with a porous medium. The fluid flow and mixed convection heat transfer of a non-Newtonian (Cu–water) nanofluid-filled circular annulus enclosure in a magnetic field are investigated Emad D. Aboud et al. [51]. Al-Amir et al. [52] studied the effect of Prandtl number on the natural heat convection inside a square cavity filled with two layers of Ag/water nanofluid-saturated porous medium and non-Newtonian fluid separated by a sinusoidal vertical interface.

An inspection of the literature has shown that thus far no study has deployed LBM to consider MHD natural convection in a square enclosure containing both a porous medium and a fluid zone. The novelty of the present investigation is simultaneous consideration of both magnetohydrodynamic and non-Darcy porous media effects, which has to the authors' knowledge not been addressed before in the literature with an LBM approach.

2. MATHEMATICAL FORMULATION

The geometry of the hybrid magnetic fuel cell is depicted in **Fig. 1.** Uniform magnetic field (B_o) is applied in the $\bar{x}$-direction and generates the perpendicular Lorentz body force. The square geometry consists of a partially filled porous zone and an adjacent free fluid zone. The horizontal walls of the computational domain are thermally insulated and left and right walls of the cavity possess different temperature gradients. In the porous zone the non-Darcy model is considered. Thermal equilibrium model is sustained between the zone I and zone II (zone I indicates porous zone and Zone II indicates fluid zone). The electrically conducting fluid (e. g. ionized Helium) is incompressible and Hall current, Maxwell displacement current and magnetic induction effects are ignored (magnetic Reynolds number is sufficiently small). The porous medium is rigid, isotropic and homogeneous. Constant thermo-physical properties of the electro-conductive fluid flow are considered except for density variation in the thermal buoyancy term i. e. Boussinesq's approximation is employed. In addition, viscous dissipation, thermal radiation, heat generation/absorption and Joule heating are neglected.

Under the foregoing assumptions, the conservation equations of momentum, mass, energy may be expressed following [22] and [25] as:

Porous layer:

Continuity:

$$\frac{\partial \overline{u}}{\partial \overline{x}} + \frac{\partial \overline{v}}{\partial \overline{y}} = 0 \tag{1}$$

x̄-momentum:

$$\rho\left[\frac{\partial\bar{u}}{\partial\bar{t}}+\bar{u}\frac{\partial\bar{u}}{\partial\bar{x}}+\bar{v}\frac{\partial\bar{u}}{\partial\bar{y}}\right]=-\frac{\partial\bar{p}}{\partial\bar{x}}+\mu\left(\frac{\partial^2\bar{u}}{\partial\bar{x}^2}+\frac{\partial^2\bar{u}}{\partial\bar{y}^2}\right)-\frac{\mu}{K}\bar{u} - \frac{1.75}{\sqrt{150}}\frac{\rho}{k^{1/2}}\bar{u}\sqrt{\bar{u}^2+\bar{v}^2} \tag{2}$$

ȳ-momentum:

$$\rho\left[\frac{\partial\bar{v}}{\partial\bar{t}}+\bar{u}\frac{\partial\bar{v}}{\partial\bar{x}}+\bar{v}\frac{\partial\bar{v}}{\partial\bar{y}}\right]=-\frac{\partial\bar{p}}{\partial\bar{y}}+\mu\left(\frac{\partial^2\bar{v}}{\partial\bar{x}^2}+\frac{\partial^2\bar{v}}{\partial\bar{y}^2}\right)-\frac{\mu}{K}\bar{v} - \frac{1.75}{\sqrt{150}}\frac{\rho}{k^{1/2}}\bar{v}\sqrt{\bar{u}^2+\bar{v}^2}-\sigma B_0^2 v+\rho g\beta\left(\bar{\theta}-\theta_c\right) \tag{3}$$

Energy:

$$\frac{\partial\bar{\theta}}{\partial\bar{t}}+\bar{u}\frac{\partial\bar{\theta}}{\partial\bar{x}}+\bar{v}\frac{\partial\bar{\theta}}{\partial\bar{y}}=\alpha\left(\frac{\partial^2\bar{\theta}}{\partial\bar{x}^2}+\frac{\partial^2\bar{\theta}}{\partial\bar{y}^2}\right) \tag{4}$$

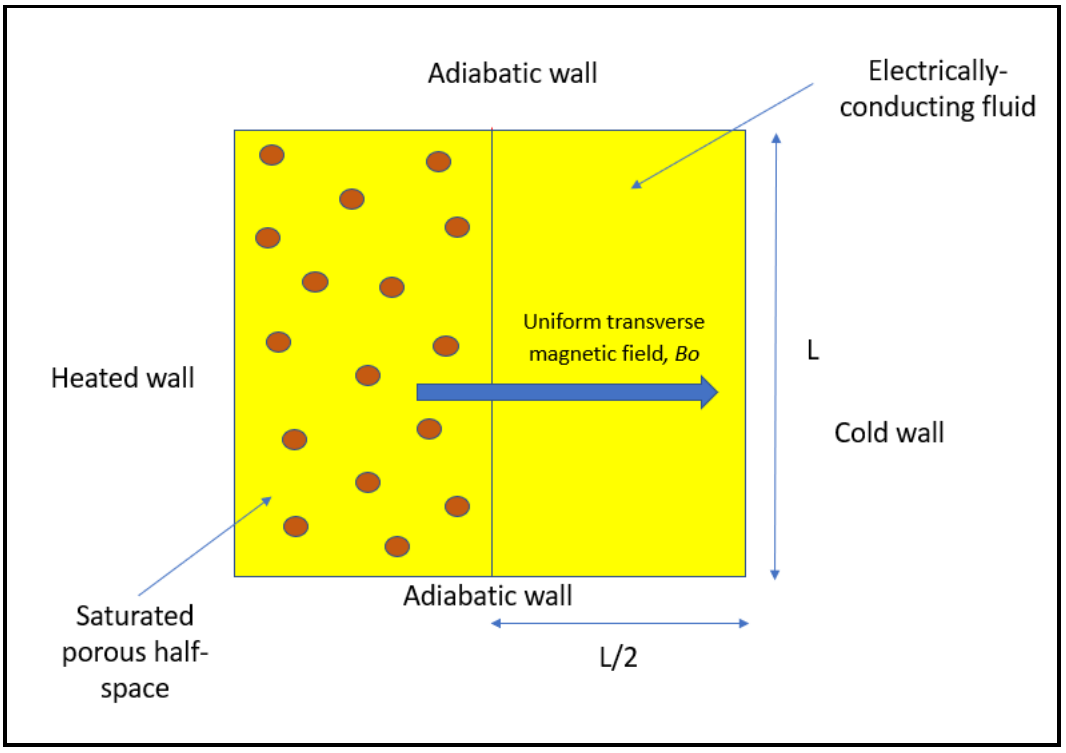

Fig. 1. Physical model for magneto-convection in partially porous enclosure.

<u>In the fluid layer:</u>

Continuity:

$$\frac{\partial \bar{u}}{\partial \bar{x}} + \frac{\partial \bar{v}}{\partial \bar{y}} = 0 \tag{5}$$

$\bar{x}$-momentum:

$$\rho\left[\frac{\partial \overline{u}}{\partial \overline{t}} + \overline{u}\frac{\partial \overline{u}}{\partial \overline{x}} + \overline{v}\frac{\partial \overline{u}}{\partial \overline{y}}\right] = -\frac{\partial \overline{p}}{\partial \overline{x}} + \mu\left(\frac{\partial^2 \overline{u}}{\partial \overline{x}^2} + \frac{\partial^2 \overline{u}}{\partial \overline{y}^2}\right) \tag{6}$$

$\bar{y}$-momentum:

$$\rho\left[\frac{\partial \overline{v}}{\partial \overline{t}} + \overline{u}\frac{\partial \overline{v}}{\partial \overline{x}} + \overline{v}\frac{\partial \overline{v}}{\partial \overline{y}}\right] = -\frac{\partial \overline{p}}{\partial \overline{y}} + \mu\left(\frac{\partial^2 \overline{v}}{\partial \overline{x}^2} + \frac{\partial^2 \overline{v}}{\partial \overline{y}^2}\right) - \sigma B_0^2 \overline{v} + \rho g \beta\left(\overline{\theta} - \theta_c\right) \tag{7}$$

Energy:

$$\frac{\partial \overline{\theta}}{\partial \overline{t}} + \overline{u}\frac{\partial \overline{\theta}}{\partial \overline{x}} + \overline{v}\frac{\partial \overline{\theta}}{\partial \overline{y}} = \alpha\left(\frac{\partial^2 \overline{\theta}}{\partial \overline{x}^2} + \frac{\partial^2 \overline{\theta}}{\partial \overline{y}^2}\right) \tag{8}$$

The boundary conditions along the solid walls are mentioned as below

On top wall $\overline{u} = \overline{v} = 0,\ \dfrac{\partial \overline{\theta}}{\partial \overline{x}} = 0$

On bottom wall $\overline{u} = \overline{v} = 0,\ \dfrac{\partial \overline{\theta}}{\partial \overline{x}} = 0$

On left wall $\overline{u} = \overline{v} = 0,\ \overline{\theta} = \overline{\theta}_H$

On right wall $\overline{u} = \overline{v} = 0,\ \overline{\theta} = \overline{\theta}_C$

Here all parameters are defined in the notation at the start of the paper. Invoking the following non-dimensional variables:

$$x = \frac{\overline{x}}{L_{ref}},\ y = \frac{\overline{y}}{L_{ref}},\ u = \frac{\overline{u} L_{ref}}{\alpha},\ v = \frac{\overline{v} L_{ref}}{\alpha},\ t = \frac{\overline{t}\alpha}{L_{ref}^2},\ p = \overline{p}\frac{L_{ref}^2}{\rho \alpha^2}$$

$$\theta = \frac{\overline{\theta} - \theta_C}{\theta_H - \theta_C},\ Ra = \frac{g\beta \Delta\theta L_{ref}^3}{\nu\alpha},\quad \Pr = \frac{\nu}{\alpha},\ \alpha = \frac{k}{\rho C_P},\ Ha = B_0 L_{ref}\sqrt{\frac{\sigma}{\mu}},\ Da = \frac{K}{L_{ref}^2} \tag{9}$$

Here again all parameters are defined in the nomenclature.

By virtue of the scaling variables in Eqn. (9), Eqns. (1)-(8) assume the dimensionless form:

<u>Porous layer</u>

$$\frac{\partial u}{\partial x}+\frac{\partial v}{\partial y}=0 \tag{10}$$

$$\frac{\partial u}{\partial t}+u\frac{\partial u}{\partial x}+v\frac{\partial u}{\partial y}=-\frac{\partial p}{\partial x}+Pr\left(\frac{\partial^2 u}{\partial x^2}+\frac{\partial^2 u}{\partial y^2}\right)-\frac{Pr}{Da}u-\frac{1.75}{\sqrt{150}}\frac{u\sqrt{u^2+v^2}}{\sqrt{Da}} \tag{11}$$

$$\begin{aligned}\frac{\partial v}{\partial t}+u\frac{\partial v}{\partial x}+v\frac{\partial v}{\partial y}=&-\frac{\partial p}{\partial y}+Pr\left(\frac{\partial^2 v}{\partial x^2}+\frac{\partial^2 v}{\partial y^2}\right)-\frac{Pr}{Da}v-PrHa^2 v\\&-\frac{1.75}{\sqrt{150}}\frac{v\sqrt{u^2+v^2}}{\sqrt{Da}}+RaPr\theta\end{aligned} \tag{12}$$

$$\frac{\partial \theta}{\partial t}+u\frac{\partial \theta}{\partial x}+v\frac{\partial \theta}{\partial y}=\frac{\partial^2 \theta}{\partial x^2}+\frac{\partial^2 \theta}{\partial y^2} \tag{13}$$

Fluid layer:

$$\frac{\partial u}{\partial x}+\frac{\partial v}{\partial y}=0 \tag{14}$$

$$\frac{\partial u}{\partial t}+u\frac{\partial u}{\partial x}+v\frac{\partial u}{\partial y}=-\frac{\partial p}{\partial x}+Pr\left(\frac{\partial^2 u}{\partial x^2}+\frac{\partial^2 u}{\partial y^2}\right) \tag{15}$$

$$\frac{\partial v}{\partial t}+u\frac{\partial v}{\partial x}+v\frac{\partial v}{\partial y}=-\frac{\partial p}{\partial y}+Pr\left(\frac{\partial^2 v}{\partial x^2}+\frac{\partial^2 v}{\partial y^2}\right)-PrHa^2 v+RaPr\theta \tag{16}$$

$$\frac{\partial \theta}{\partial t}+u\frac{\partial \theta}{\partial x}+v\frac{\partial \theta}{\partial y}=\frac{\partial^2 \theta}{\partial x^2}+\frac{\partial^2 \theta}{\partial y^2} \tag{17}$$

The transformed boundary conditions may be stated as follows:

$u=v=\dfrac{\partial \theta}{\partial y}=0$ for $y=0,l$ and $0\le x\le l$

$\theta=1, u=v=0$ for $x=0$ and $0\le y\le l$

$\theta=0, u=v=0$ for $x=l$ and $0\le y\le l$

At $X = l/2$, *and* $0 < Y < 1$

$$u_{porous} = u_{non-porous},\ v_{porous} = v_{non-porous}$$
$$p_{porous} = p_{non-porous}, \theta_{porous} = \theta_{non-porous} \quad (18)$$

3. LATTICE BOLTZMANN METHOD (LBM) NUMERICAL SOLUTION

The LBM in this study uses a Lattice Boltzmann equation with a linearized collision term in which the Bhatnagar-Gross-Krook (BGK) approximation is deployed. The general form of the conservation equations in either the porous medium or fluid layer can then be stated as follows:

$$\rho\left[\frac{\partial \bar{u}}{\partial \bar{t}} + \bar{u}\frac{\partial \bar{u}}{\partial \bar{x}} + \bar{v}\frac{\partial \bar{u}}{\partial \bar{y}}\right] = -\frac{\partial \bar{p}}{\partial \bar{x}} + \mu\left(\frac{\partial^2 \bar{u}}{\partial \bar{x}^2} + \frac{\partial^2 \bar{u}}{\partial \bar{y}^2}\right) + F_x \quad (19)$$

$$\rho\left[\frac{\partial \bar{v}}{\partial \bar{t}} + \bar{u}\frac{\partial \bar{v}}{\partial \bar{x}} + \bar{v}\frac{\partial \bar{v}}{\partial \bar{y}}\right] = -\frac{\partial \bar{p}}{\partial \bar{y}} + \mu\left(\frac{\partial^2 \bar{v}}{\partial \bar{x}^2} + \frac{\partial^2 \bar{v}}{\partial \bar{y}^2}\right) + F_y \quad (20)$$

$$\frac{\partial \theta}{\partial t} + u\frac{\partial \theta}{\partial x} + v\frac{\partial \theta}{\partial y} = \left(\frac{\partial^2 \theta}{\partial x^2} + \frac{\partial^2 \theta}{\partial y^2}\right) \quad (21)$$

Here the following notation applies for the porous media drag forces and Lorentzian hydromagnetic drag:

$$F_x = -\frac{Pr}{Da}\bar{u} - \frac{1.75}{\sqrt{150Da}}\bar{u}\sqrt{\bar{u}^2 + \bar{v}^2} \quad (22)$$

$$F_y = -\frac{Pr}{Da}\bar{v} - \frac{1.75}{\sqrt{150Da}}\bar{v}\sqrt{\bar{u}^2 + \bar{v}^2} - Ha^2 Pr\bar{v} + RaPr\theta \quad (23)$$

The two-dimensional Lattice-Boltzmann model with D2Q9 lattices is adopted to compute the flow field as depicted in **Fig. 2.**

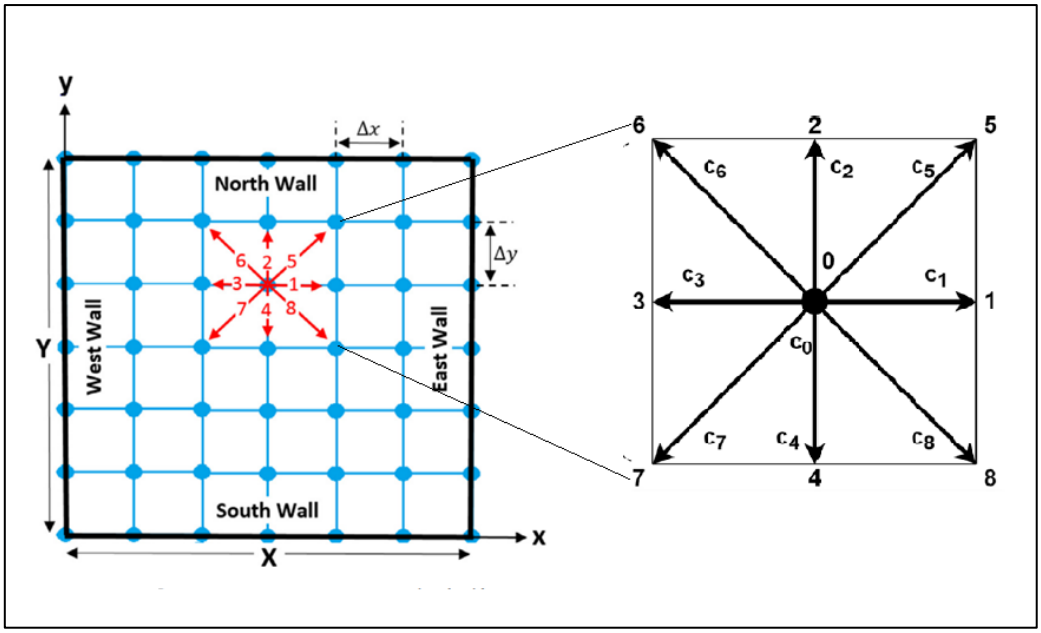

Fig. 2. Schematic diagram of computational grid and D2Q9 lattice model

The flow field and distribution function (see Fig. 3) of the Bhatnagar-Gross-Krook (BGK) approximation can be expressed as follows [26, 27]:

$$f_i\left(x+C_i\Delta t,t+\Delta t\right)=f_i\left(x,t\right)-\frac{1}{\tau_\alpha}\left(f_i\left(x,t\right)-f_i^{eq}\left(x,t\right)\right)+\Delta tF_i \tag{24}$$

$$f_i^{eq}=w_i\rho\left[1+\frac{3(C_iu)}{C_S^2}+\frac{9(C_iu)^2}{2C_S^4}-\frac{3u^2}{2C_S^2}\right] \tag{25}$$

Here *x*, denotes the position of the fluid particle and Δt denotes the time step.

Also, the weighting coefficients are:

$$w_i=\begin{cases}\dfrac{4}{9},i=0\\ \dfrac{1}{9},i=1,2,3,4\\ \dfrac{1}{36},i=5,6,7,8\end{cases} \tag{26}$$

In the same way, the equilibrium distribution function addressing the thermal energy distribution g_i^{eq}

Here $C_S = \frac{c}{\sqrt{3}}$ refers to the speed of the sound in the fluid flow field and $c = \delta x/\delta t$ expresses the streaming speed. Also, $\boldsymbol{e_i}$ represents the velocity in the D2Q9 lattice for the discrete type, (as shown in **Fig. 2**) and is expressed as [26]:

$$e_{\mathbf{i}} = \begin{cases} 0 & i = 0 \\ (\cos[(i-1)\pi/2], \sin[(i-1)\pi/2])c & i = 1,2,3,4 \\ \sqrt{2}\left(\cos[(i-5)\pi/2 + \pi/4], \sin[(i-5)\pi/2 + \pi/4]\right)c & i = 5,6,7,8 \end{cases} \quad (27)$$

F_i refers the external force and it is defined as:

$$F_i = w_i\left(1 - \frac{1}{2\tau}\right)\left[3\left(\bar{e}_i.\bar{F}\right) + 9\left(\bar{e}_i.\bar{u}\right)\left(\bar{e}_i.\bar{F}\right) - 3\left(\bar{u}.\bar{F}\right)\right] \text{ and } \bar{F} = -\frac{\upsilon}{\kappa}\bar{U} - \frac{C_F}{\sqrt{\kappa}}\left|\bar{U}\right|\bar{U} + G \quad (28)$$

Here:

$$C_k = \frac{1.75}{\sqrt{150}}$$
$$\kappa = \frac{d_p^2}{150(1-\varepsilon)^2} \quad (29)$$

G represents the body force due to gravity:

$$G = g\beta\left(T - T_c\right)j \quad (30)$$

The *distribution function* for temperature (thermal field) is defined as follows:

$$g_i\left(x + C_i\Delta t, t + \Delta t\right) = g_i\left(x,t\right) - \frac{1}{\tau_\alpha}\left(g_i\left(x,t\right) - g_i^{eq}\left(x,t\right)\right) \quad (31)$$

$$g_i^{eq} = w_i' g\left[1 + 3\frac{C_i u}{C_S^{\,2}}\right] \quad (32)$$

The relaxation times for thermal diffusivity α and kinematic viscosity v are defined as follows:

$$\alpha = \left[\tau_\alpha - \frac{1}{2}\right]c_s^{\,2}\Delta t \quad , \quad \nu = \left[\tau_\nu - \frac{1}{2}\right]c_s^{\,2}\Delta t \quad (33)$$

Macroscopic quantities ρ , u and T can be calculated using [26]:

$$\rho = \sum_i f_i \tag{34}$$

$$\rho u = \sum_i f_i \mathbf{c}_\mathbf{i} \tag{35}$$

$$\theta = \sum_i \mathrm{g}_i \tag{36}$$

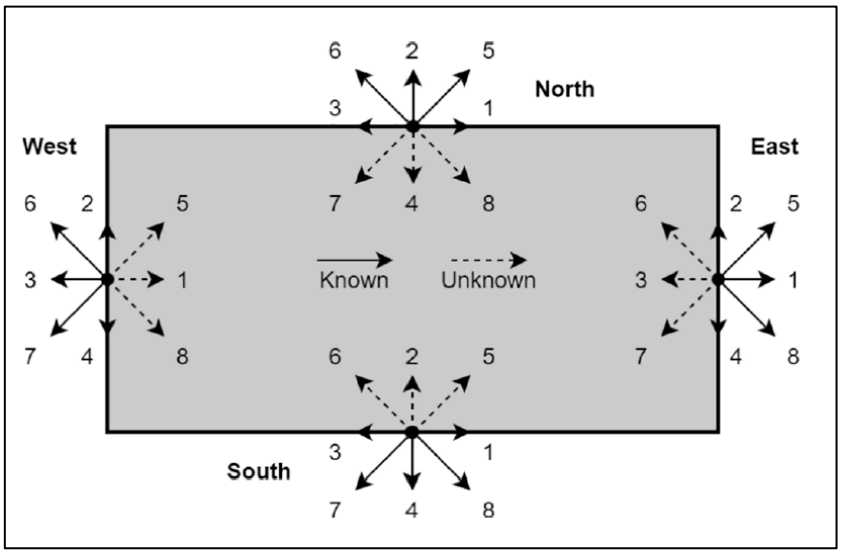

Fig. 3. Distribution functions at the wall boundaries

3.1 Boundary conditions:

Bounce-back conditions are applied on the enclosure boundaries (non-moveable walls) – see Fig. 3 for the distribution functions at the enclosure walls.

For the left, right, top and bottom walls, respectively, we have.

for all the nodes on the east boundary

$f_3(x, y) = f_1(x, y)$

$f_6(x, y) = f_8(x, y)$ (37a,b,c)

$f_7(x, y) = f_5(x, y)$

for temperature field on the west boundary

$g_1(x, y) = \bar{\theta}_H \ (\omega_1 + \omega_3) - g_3(x, y)$

$g_5(x, y) = \bar{\theta}_H \ (\omega_5 + \omega_7) - g_7(x, y)$ (38 a,b,c)

$g_8(x, y) = \bar{\theta}_H \ (\omega_8 + \omega_6) - g_6(x, y)$

For the adiabatic walls, i. e. both North and South boundaries

$g_4(x, y) = g_2(x, y)$

$g_7(x, y) = g_5(x, y)$ (39 a,b,c)

$g_8(x, y) = g_6(x, y)$

LBM simulation works well for flows of incompressible fluids for which *Mach* number (*Ma*) must be less than 0.3. Hence in the computations, the Mach number is fixed to 0.1. Now by fixing the Ra number, with the selected working fluid Prandtl number (*Pr*) and Mach number, the kinematic viscosity and thermal diffusivity are calculated as follows:

$$\nu = M.C_s.Ma\sqrt{\frac{\mathrm{Pr}}{Ra}}$$
$$\alpha = \frac{\nu}{\mathrm{Pr}} \quad \text{(40 a,b)}$$

Here *M* denotes the number of lattices in the *y* direction.

The local Nusselt number along the isothermal side walls is given by the expression:

$$Nu = -\left(\frac{\partial\theta}{\partial X}\right)\Big|_{X=0,1} \quad (41)$$

The average Nusselt number is evaluated as follows

$$Nu = -\int_0^L \left(\frac{\partial\theta}{\partial X}dY\right)\Big|_{X=0,1} \quad (42)$$

Table. 1. Grid independence and validation for average Nusselt number (*Nu*) with *Pr* = 0.71

Ra	Nu	Bég *et al* [39]	de Vahl Davis [40]	Wan *et al.* [41] FEM	Present study 41X41	Present study 61X61	Present study 81X81	Present study 101X101
10^4	Average	2.2526	2.242	2.254	2.2526	2.2455	2.2444	2.2442

4. GRID INDEPENDENCE AND VALIDATION

The MATLAB-based LBM code has been tested for grid independence for the average Nusselt number (*Nu*). The grid size (101*101) was confirmed to provide a grid-independent solution as shown in **Table 1**. The accuracy of the LBM code is high and provides excellent precision for the studied regime. Validations of present LBM with earlier studies conducted by Bég *et al* [39] (using a MAC finite difference code), de Vahl Davis [40], and Wan *et al.* [41] (who used a finite element method) are also addressed in **Tables 1 and 2**. The comparisons are conducted for incompressible non-magnetic fluid in the absence of thermal radiative effects i.e. $Pr = 0.71$ (air), $Ha = Rd = 0$, and $Da \to \infty$. A good correlation is found with 101X101 lattice nodes.

Table. 2. Comparison of average Nusselt number.

Ra	*Nu*						
	Bég *et al.* [39]	de Vahl Davis [40]	Wan *et al.* [41]	Present LBM	Error % [41]	Error % [40]	Error % [39]
Ra= 10^4	2.2526	2.242	2.254	2.2442	0.4347	0.09813	0.3729
Ra=10^5	4.5907	4.523	4.598	4.5947	0.0718	1.58523	0.0871
Ra=10^6	8.9905	9.035	8.976	8.9821	0.0679	0.5855	0.0934

5. RESULTS AND DISCUSSION

Figs 4-14 illustrate contour plots and graphs for streamlines, temperature contours (isotherms), local Nusselt number on the left and right walls and mid-section secondary velocity profiles computed with the present MATLAB-based LBM code. Data is depicted based on magnetizable Helium gas (Pr = 0.71), low impact of magnetic field (Ha = 5.0), relatively low permeability porous media (Da = 0.001), and strong thermal buoyancy (Ra= 10^5), unless otherwise indicated.

Fig. 4 shows that increasing Darcy number, the left porous zone becomes increasingly heated. The initial single vortex cell in the purely fluid right space computed in Fig 4(a) Da = 0.0001 merges increasingly into the left porous medium half space in figure (b) Da = 0.001. A tenfold increase in Darcy number implies a tenfold increase in permeability in the porous zone. Both the Darcian and Forchheimer body forces in the primary and secondary momentum Eqns. (11) and (12) are inversely related to Darcy number. These forces are strongly reduced, and momentum development is encouraged i. e. flow acceleration is produced in the porous zone. The fluid zone does not feature these porous drag forces. The intensity of streamlines in the porous zone is increased as more Helium gas percolates into the left half space. At the upper and lower horizontal boundaries, intensification is also observed in streamlines. With further increase in Darcy number to Fig 4 (c) Da = 0.01 and then Fig. 4(d) Da = 0.1, the boost in permeability also induces a lateral expansion of the single vortex cell further towards the left hot wall. The initial strong asymmetry computed at lower Darcy numbers is further reduced in Fig. 4(d) where for very high permeability, the vortex cell is diagonally stretched between the upper left corner and lower right corner and bifurcates into a double vortex structure which is more flattened towards the left and right wall but much sharper in the core of the enclosure. Darcy number therefore exerts a profound effect on the internal flow circulation and even with only partial (half) filling of the enclosure with porous material, a much more homogenous flow distribution is produced indicating more efficient circulation in the fuel cell.

Fig. 5 illustrates the response in temperature distribution (isotherms) with increasing Darcy number. At low Darcy number i. e. very low permeability (Fig. 5a), isotherms are essentially vertical in the left porous half space and cool from the left hot wall progressively towards the core section interface with the fluid zone. At the inception of the purely fluid zone, much cooler isotherms are observed, and they are significantly distorted towards the top right corner and remain blue (cold) throughout the right half space to the cold right wall. As Darcy number increases there is a systematic encroachment of hotter isotherms into the central zone of the enclosure and intensification (heating) further along the upper adiabatic wall, although cooler zones are sustained along the right vertical (cold) wall and the lower boundary. At highest Darcy number (Fig. 5d i. e. Da = 0.1), the warmer central zone is expanded. In other words, the higher permeability in the left half space encourages thermal diffusion and permits hotter percolating fluid from the left wall to penetrate deeper into the core of the enclosure. Central isotherms morph from initially vertical topologies to horizontal topologies extending across the breadth of the enclosure.

Fig. 6 shows the evolution in streamlines in the enclosure with an increment in Hartmann number. As noted earlier, magnetic body force arises only in the secondary momentum Eqn. (12) for the porous zone and the equivalent eqn. (16) for the purely fluid zone. In both equations, the Lorentzian magnetic force is linear, $-\mathrm{PrHa}^2\mathrm{v}$, and is a retarding force. At low Hartmann number, $Ha = B_0 L_{ref}\sqrt{\frac{\sigma}{\mu}}$, which says Lorentzian force in the regime, the left porous zone exhibits a slight distortion in the central section whereas there is a discrete vortex cell in the right purely fluid zone. As Ha is increased from 5.0 (Fig. 6a) and the Lorentzian force is amplified significantly in Figs. 6 (b) Ha = 20 (c) Ha = 30 and (d) Ha = 50, the initially vertically stretched single cell in the right space is stretched laterally and diagonally between the upper right corner and lower left corner. The cell is elongated diagonally and there is a reduction in streamline intensity engulfing the cell indicating that significant damping of the flow is produced with stronger magnetic field. The streamlines at the boundaries are increasingly constricted owing to momentum re-distribution at the walls. The overall effect of stronger magnetic field is however to decelerate the core flow in the enclosure.

Fig. 7 illustrates the effect of Hartmann magnetic number (Ha) on isotherms. As Hartmann number increases from (a)Ha = 5.0 (b) Ha = 20 (c) Ha = 30 to a maximum value of (d) Ha = 50, there is a progressive heating in the core region of the enclosure. Topologies of isotherms remain asymmetric and are skewed towards the upper right corner and lower left corner of the enclosure. The top and left walls exhibit higher temperatures whereas there are much cooler zones at the right and lower horizontal wall. The increase in magnetic field essentially influences principally the core of the enclosure. As magnetic field is increased, i. e. Hartmann number is elevated, supplementary work is required to drag the electrically conducting fluid against the action of the vertically orientated Lorentzian drag force, $-\mathrm{PrHa}^2\mathrm{v}$. This extra work expended is degenerate as thermal energy which heats the core region of the enclosure. There are higher temperatures computed at the lower section of the porous left half space and the upper section of the purely fluid right half space. Isotherms are also increasingly constricted towards the lower left hot wall and upper right cold wall with progressive increase in Hartmann magnetic number. Clearly thermal diffusion is modified in the enclosure with stronger magnetic field and a more homogenous hotter zone is achieved in the core section, which would imply that thermal efficiency is actually boosted in the fuel cell, concurring with experimental findings reported in Abdel-Rehim [5] among others.

Fig.8 shows the influence of Hartmann magnetic number (Ha) on streamlines at a much higher Darcy number (Da = 0.1) i. e. much higher permeability, compared with Fig. 6 (Da = 0.001): (a) Ha = 0.0 (b) Ha = 20 (c) Ha=30 (d) Ha=50. Significantly different internal vortex structures are observed. In the absence of magnetic field (Fig. 8a), a dual structure is now observed in which both porous and fluid zones exhibit a single vortex which are inclined from the upper left corner to the lower right corner of the enclosure. Non-conducting flow therefore achieves a more homogenous internal flow structure than the magnetohydrodynamic flow case in Fig. 6(a). With progressive increase in Hartmann number, the two vortex cells merge centrally, and the single elongated cell begins to rotate anti-clockwise. For Fig. 8(b) this single central vortex is laterally expanded and in Fig 8(c) it is tilted clearly from the upper right corner towards the lower left corner. The single vortex further rotates anti-clockwise for maximum Hartmann number (Ha = 50) as observed in Fig. 8(d) although it is more constricted and stretched to a greater extent from the upper right corner to the lower left corner of the enclosure. There is clearly an interplay between the permeability of the left half space porous zone and the action of the transverse magnetic field. Internal flow structure in the fuel cell can therefore demonstrably be manipulated with judicious selection of the porous medium permeability and the deployment of a stronger magnetic field, which changes the vortex cell distribution and orientation within the enclosure.

Fig.9 displays shows the influence of Hartmann magnetic number (Ha) on isotherms again at a much higher Darcy number (Da = 0.1) i. e. much higher permeability, compared with Fig. 7 (Da = 0.001): (a) Ha = 0.0 (b) Ha = 20 (c) Ha=30 (d) Ha=50. Similar topologies are computed at higher Hartmann number i. e. Figs. 8 (b), (c), (d) to those in computed earlier in Figs. 6(b), 9c) and (d), although the central hotter isotherms extend further towards the right cold wall. In the absence of magnetic field (Fig. 8a) the hotter (yellow and green) temperature contours extend more deeply from the top wall into the core of the enclosure and isotherms are largely horizontal whereas in Fig. 6(a) they are essentially more vertical in the left half space (porous zone). There is also a greater distortion of isotherms near the lower base wall although a cooler zone is sustained there. Cooler (blue) isotherms are more strongly clustered towards the right cold wall also at all Hartmann numbers. The higher permeability (greater Da value) will clearly encourage the spreading of heat through the porous left zone and this in conjunction with the magnetic field intensity, modifies the transmission of heat through the core of the enclosure. The implication is that again via careful selection of permeability for the porous left half space

material and applied transverse magnetic field intensity, heat transfer characteristics within the enclosure can be regulated and optimized for fuel cell designs.

Fig. 10 depicts the impact of Rayleigh number (Ra) on streamlines for Da = 0.001, Ha = 5.0: (a) Ra = 10^3(b) Ra = 10^4 (c) Ra = 10^5 (d) Ra = 10^6. At low Ra value (Fig 10a, b), weak circulation is computed in the left porous half space and a strong single vertically elongated vortex cell is observed in the purely fluid right half space. Much stronger circulation is computed therefore in the right half space. However, with progressive increase in Ra to (c) Ra = 10^5 (d) Ra = 10^6, the right vortex cell is increasingly expanded laterally, contracts vertically and penetrates deeper into the left porous half space. Significant distortion in streamlines is observed in the core zone at maximum Rayleigh number. Clearly the increase in thermal buoyancy accelerates the flow in the core of the enclosure (cavity) and leads to a more homogenous vorticity distribution across the enclosure, although asymmetry is still present. Thermal buoyancy force arises in both Eqns. (12) and 916) for both porous and fluid zones i. e. $+\mathrm{Ra}\,\mathrm{Pr}\,\theta$. Unlike the Lorentzian magnetic body force, thermal buoyancy force is an assistive force which encourages momentum development in the regime and accelerates the flow principally in the core section. Natural convection therefore boosts flow acceleration and this will also enhance efficiency in the hybrid fuel cell configuration.

Fig. 11 shows the impact of Rayleigh number (Ra) on isotherms for Da = 0.001, Ha = 5.0: (a) Ra = 10^3 (b) Ra = 10^4 (c) Ra = 10^5 (d) Ra = $10^{6.}$ At low Rayleigh number, (Fig. 11a), thermal buoyancy is weaker, and the isotherms are essentially vertical through both the left half porous space and right fluid zone. Much higher temperatures are observed naturally near the left hot wall and there is a progressive cooling through the enclosure towards the right cold wall. Intermediate temperatures are computed in the central (core) zone i. e. green contours. As Ra increases, thermal buoyancy is accentuated, and the temperature contours become distorted towards the lower left corner and. upper right corner. There is an expansion of the hotter zone further along the upper wall and with further increment in Rayleigh number, the warmer contours push increasingly into the core zone with a larger upper warm zone and essentially horizontal isotherms in the core zone. The right wall and lower base wall remain however much cooler (blue contours). Effectively thermal buoyancy encourages the transport of heat under natural convection currents throughout the core of the enclosure leading to higher thermal efficiency.

Fig. 12 shows the evolution of local Nusselt number at (a) Left wall (b) Right wall, with increment in Darcy number (Da) for Ha = 5.0 and Ra = 10^5. With greater Darcy number, Nusselt number is boosted at the left hot wall and also increases with descent towards the lower adiabatic boundary i. e. decreasing Y values. Heat transfer to the wall is boosted with greater permeability since convective heat transfer is elevated relative to conductive heat transfer for more permeable materials (less solid fibers present in the left half space porous zone). This manifests in an escalation in Nusselt number. Similarly at the right (cold) wall there is also an enhancement in Nusselt number with Darcy number, although Nusselt number is found to increase with ascent towards the upper adiabatic boundary i. e. increasing Y values (the opposite trend to the left hot wall).

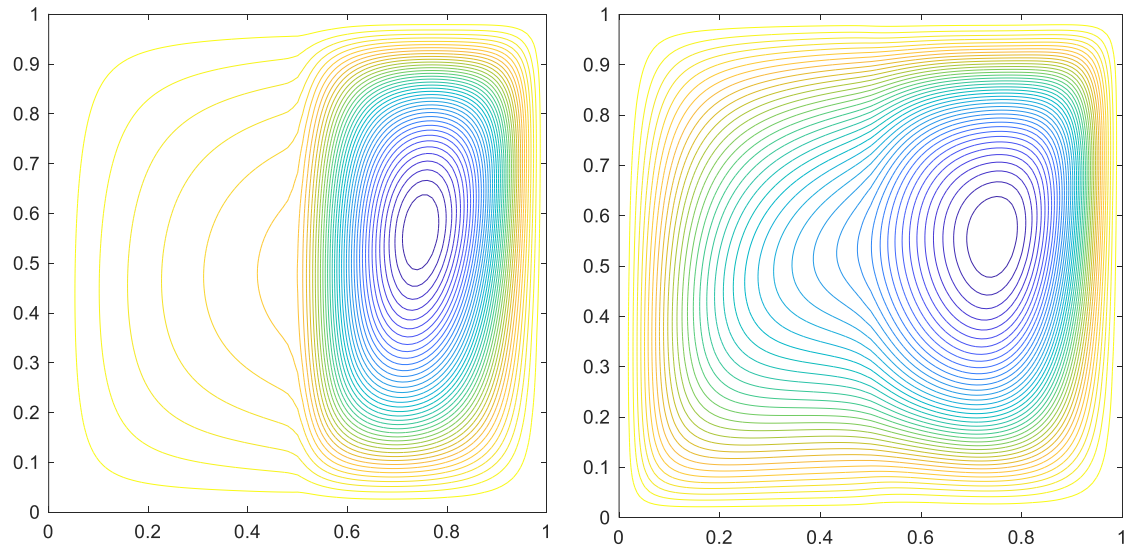

(a) (b)

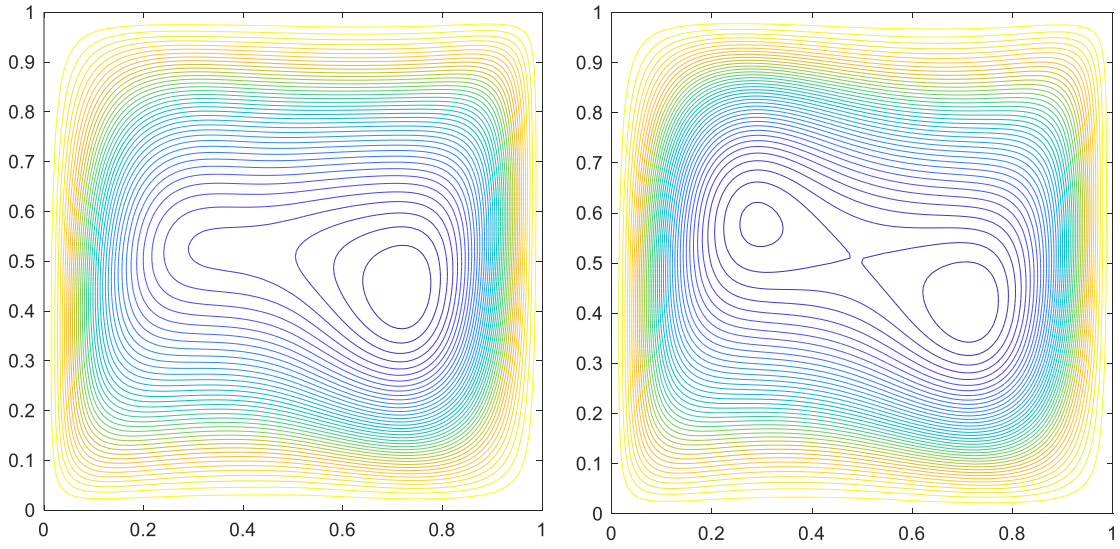

(c) (d)

Fig.4. The impact of Darcy number on streamlines with *Ra= 10^5 and Ha = 5.0:* (a) *Da = 0.0001 (b) Da = 0.001 (c) Da = 0.01 (d) Da = 0.1.*

Fig. 13 illustrates the distribution of local Nusselt number at (a) Left wall (b) Right wall, with increment in Rayleigh number (Ra) for Ha = 5.0 and Da=0.1. With greater Rayleigh number, Nusselt number is also strongly boosted at the left hot wall (Fig. 13a) and also increases with descent towards the lower boundary i.e. decreasing Y values. Heat transfer to the left hot wall is clearly enhanced with greater Rayleigh number (stronger thermal buoyancy). Clearly the increase in thermal buoyancy accelerates the flow in the core of the enclosure (cavity) and leads to a more homogenous vorticity distribution across the enclosure, although asymmetry is still present. Thermal buoyancy force arises in both Eqns. (12) and (16) for both porous and fluid zones i. e. $+Ra\,Pr\,\theta$. Unlike the Lorentzian magnetic body force, thermal buoyancy force is an *assistive* force which encourages momentum development in the regime and accelerates the flow principally in the core section. At the right cold wall (Fig. 13b) there is a strong increase in Nusselt number also with increment in Rayleigh number. However, once again the Nusselt number increases at the cold wall with higher values of Y i.e. with progressive ascent, unlike at the left hot wall.

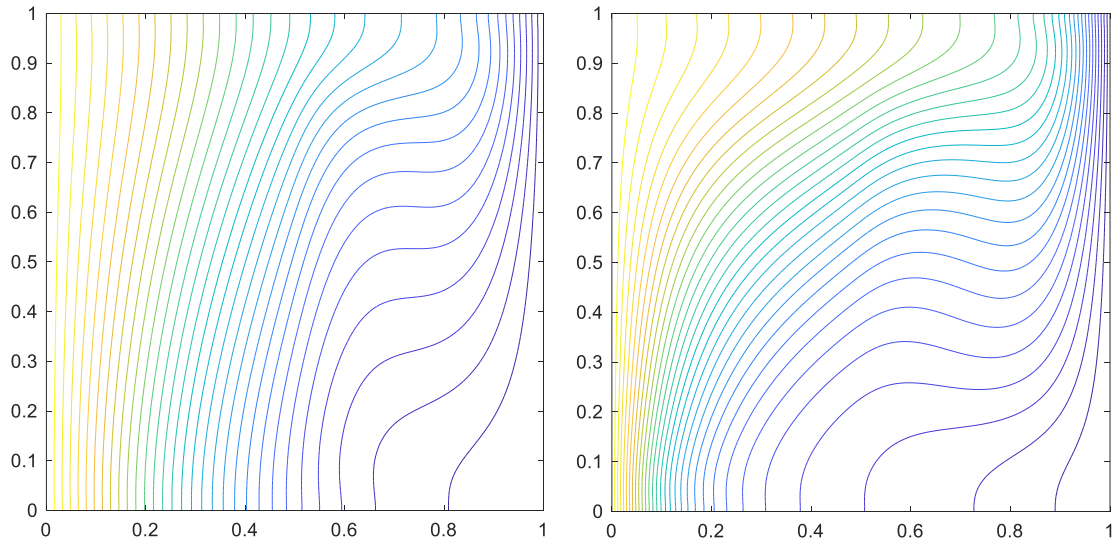

(a) (b)

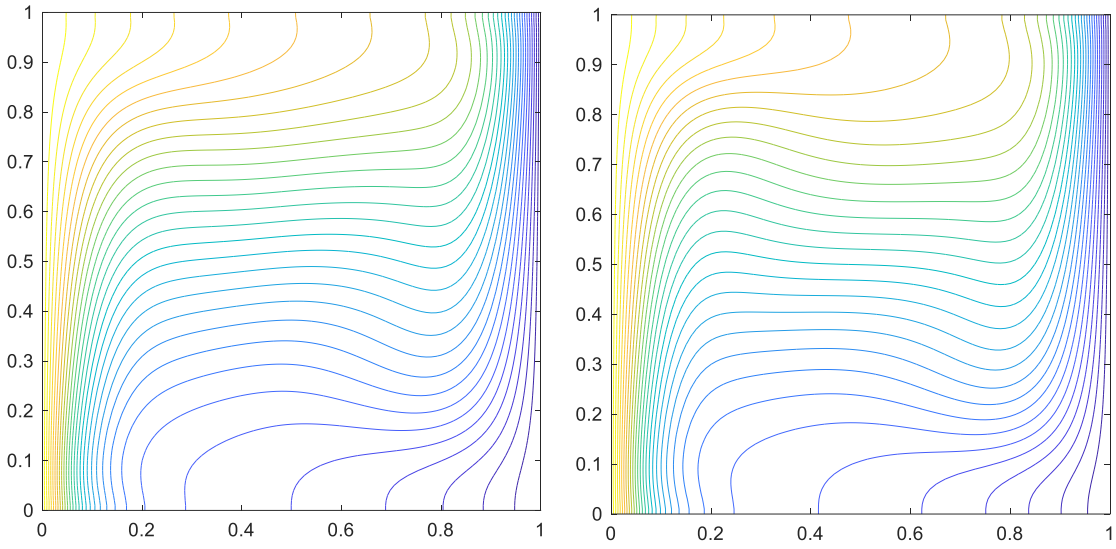

(c) (d)

Fig.5. The influence of Darcy number (Da) on isotherms with *Ra= 10^5 and Ha = 5.0*: (a) *Da = 0.0001 (b) Da = 0.001 (c) Da = 0.01 (d) Da = 0.1.*

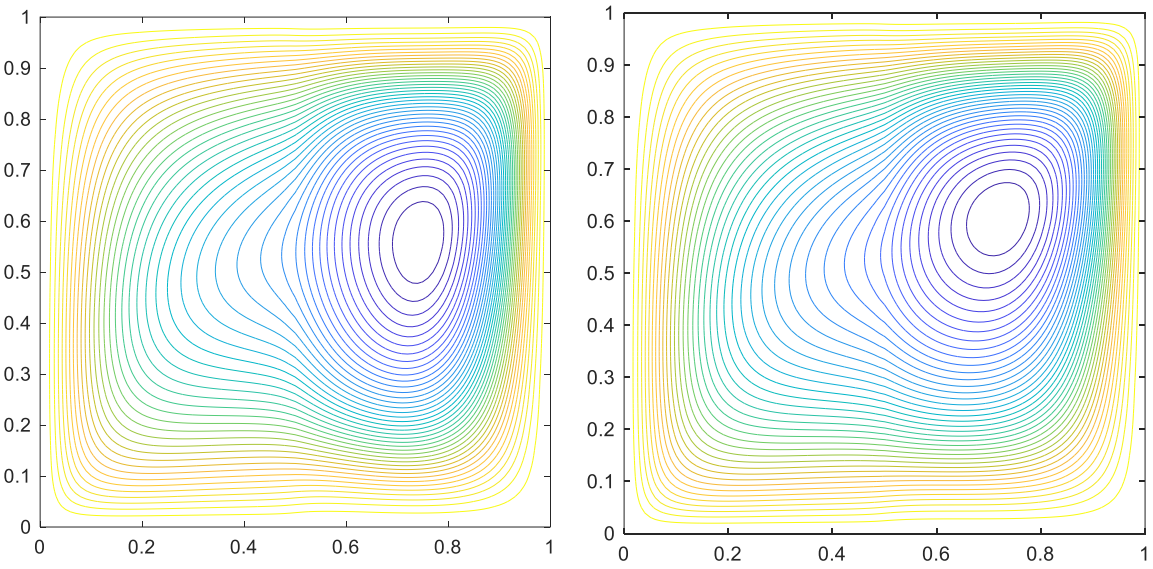

(a) (b)

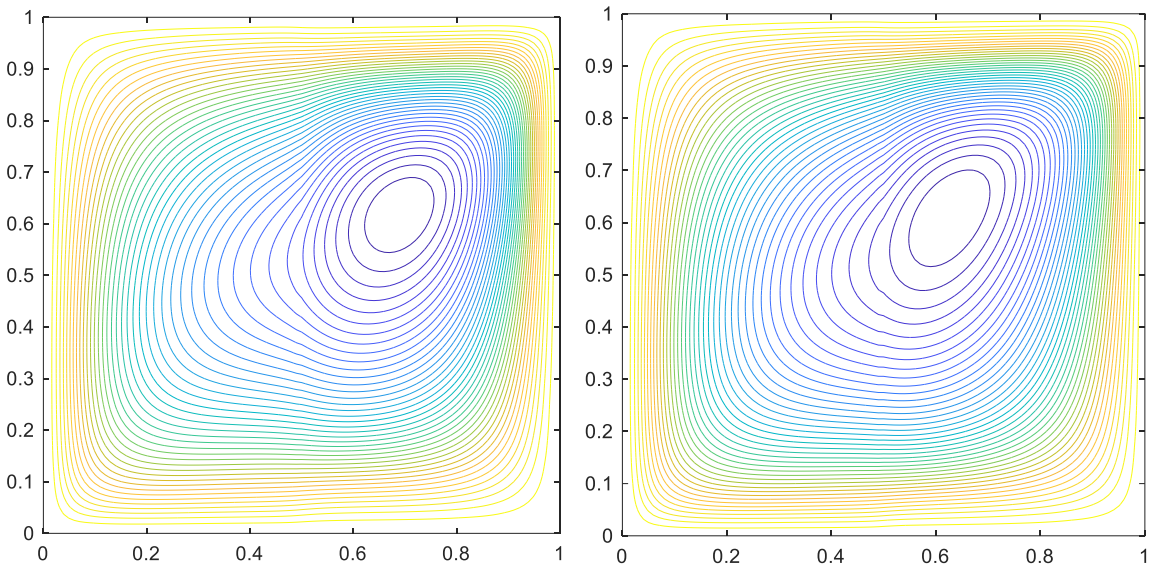

(c) (d)

Fig.6. The influence of Hartmann magnetic number (*Ha*) on streamlines for Ra= 10^5, Da = 0.001: (a)*Ha = 5.0, (b) Ha = 20 (c) Ha = 30 (d) Ha = 50.*

Fig. 14 shows the impact of Darcy number on horizontal centre line *secondary velocity profile (V)* for *Ra = 10^5 and Ha = 5.0*. In the left porous zone (0 < X < 0.5) there is initially a strong increase in centre line secondary velocity at low values of X, with increasing Darcy number, although at higher values it is suppressed. A tenfold increase in Darcy number implies a tenfold increase in permeability in the porous zone. Both the Darcian and Forchheimer body forces in the primary and secondary momentum Eqns. (11) and (12) are inversely related to Darcy number. These forces are strongly reduced, and momentum development is encouraged i. e. flow acceleration is produced in the porous zone. The fluid zone does not feature these porous drag forces. The intensity of streamlines in the porous zone is increased as more Helium gas percolates into the left half space.

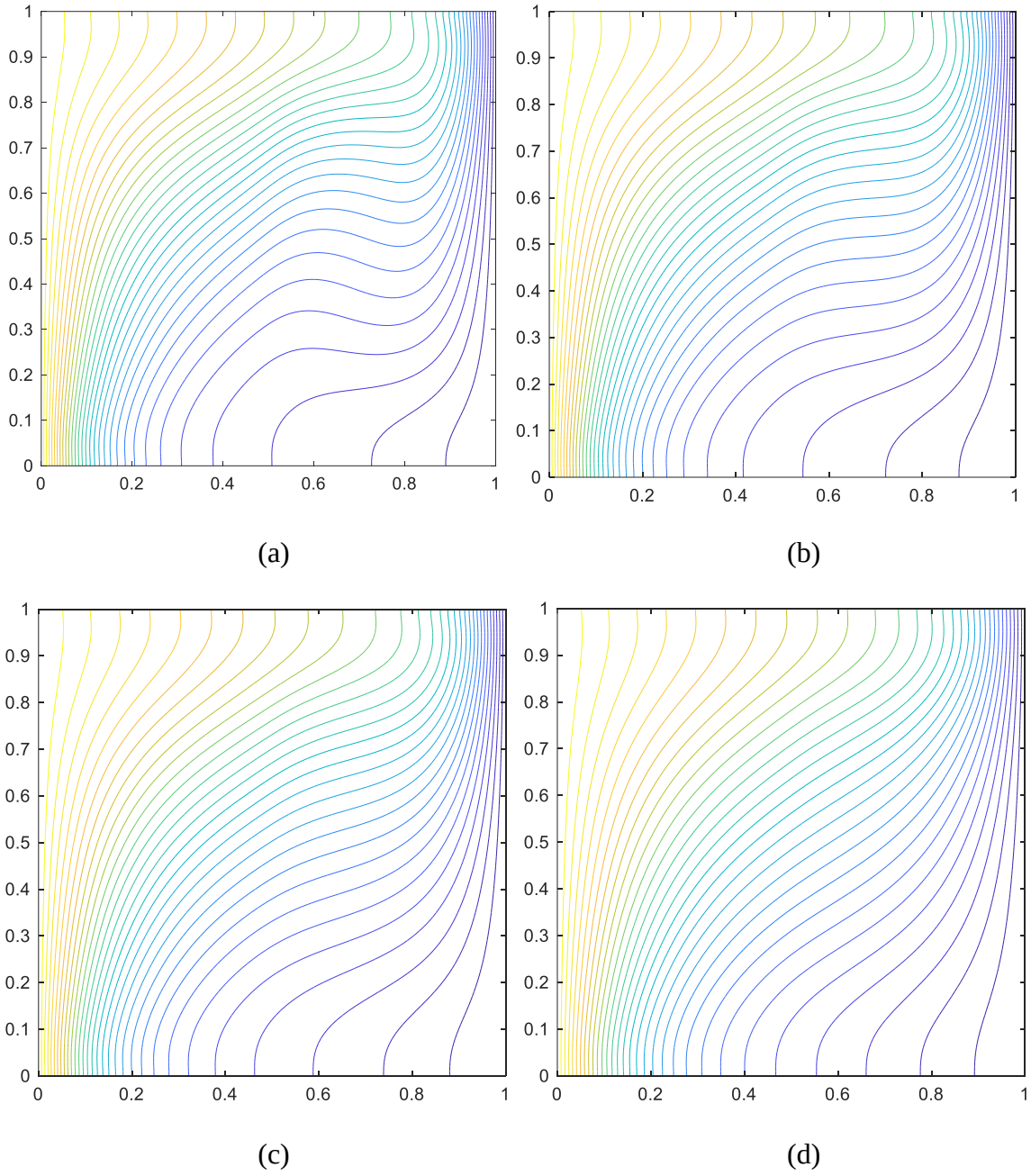

Fig.7. The influence of Hartmann magnetic number (*Ha*) on isotherms for Ra= 10^5, Da = 0.001: *(a)Ha = 5.0 (b) Ha = 20 (c) Ha = 30 (d) Ha = 50.*

In the right fluid zone (0.5<X<1.0), initially increasing Darcy number reduces secondary velocity which eventually becomes negative indicating flow reversal. While the porous medium is present only in the left half space, the greater permeability with increasing Darcy number influences the penetration of electrically conducting Helium gas into the right fluid zone also. Therefore, while secondary flow acceleration is produced in the left half space with

greater Darcy number, the opposite effect i.e., retardation is generated in the right fluid zone. The deployment of a partial porous medium in the enclosure therefore can be exploited to influence flow characteristics in the entire enclosure.

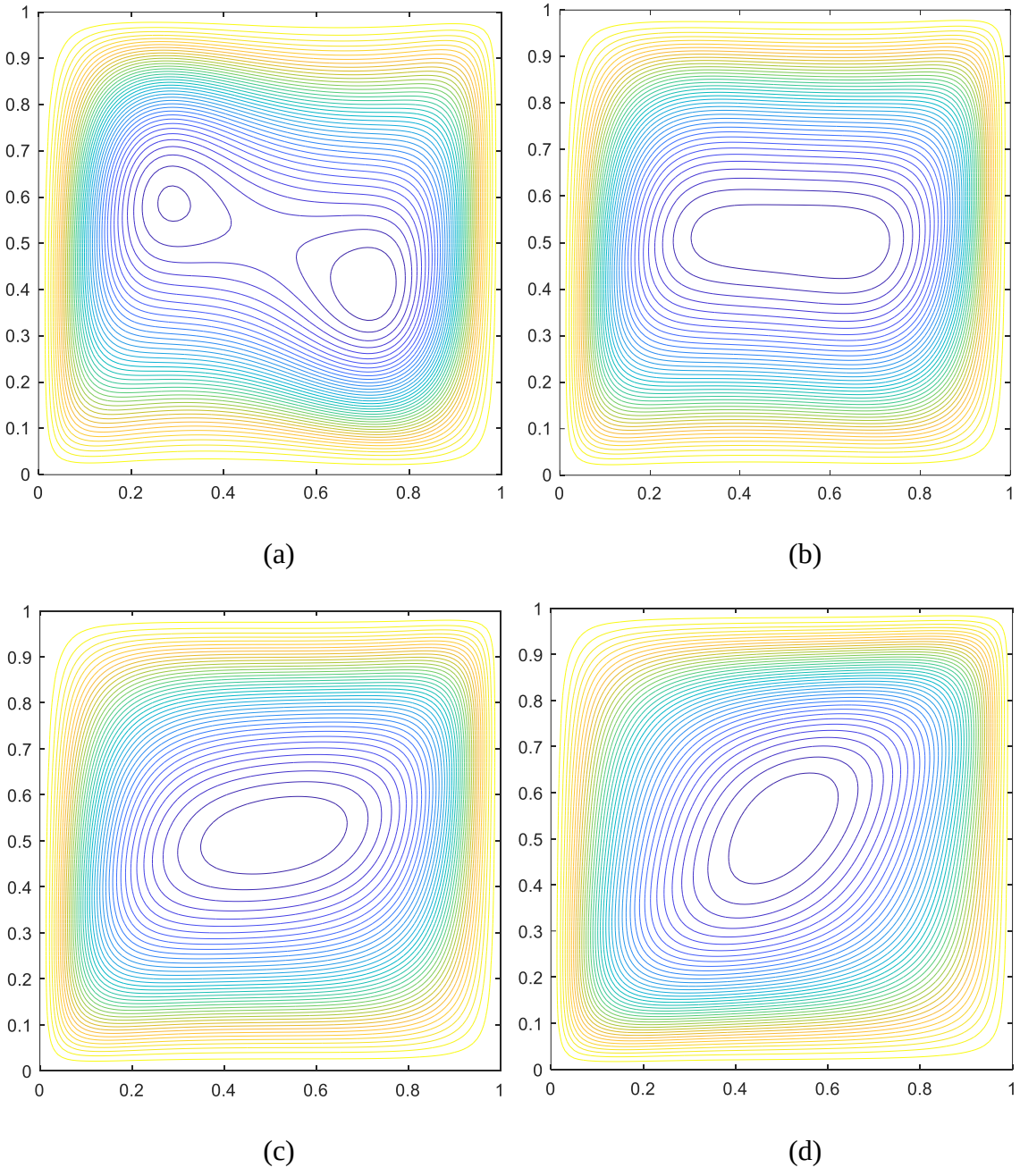

Fig.8 The influence of Hartmann magnetic number (*Ha*) on streamlines for Ra= 10^5, Da = 0.1 (higher permeability): (a) *Ha = 0.0 (b) Ha = 20 (c) Ha=30 (d) Ha=50.*

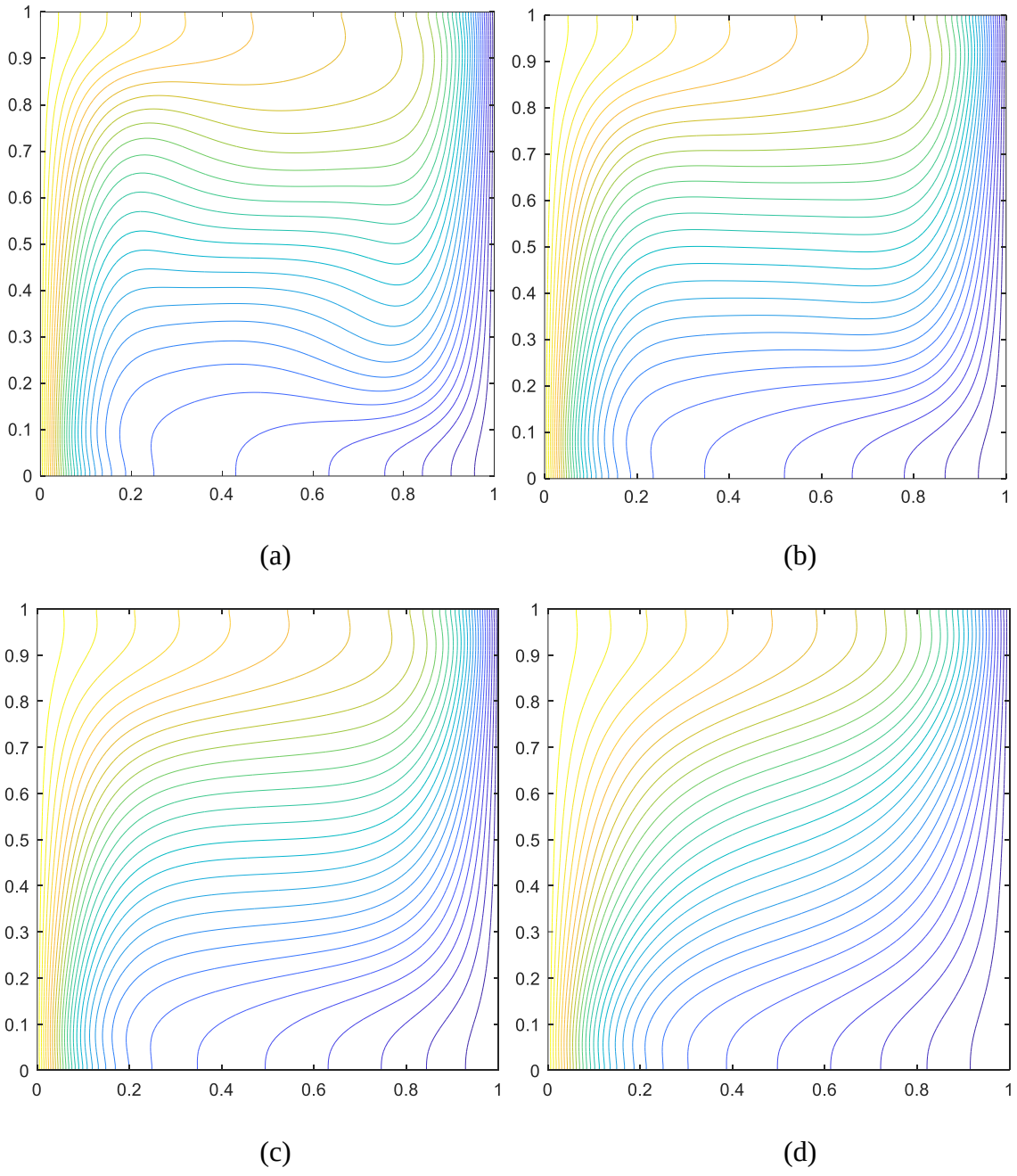

Fig. 9. The impact of Hartmann number (*Ha*) on isotherms for Ra= 10^5, Da = 0.1 (higher permeability): (a)*Ha = 0.0 (b) Ha = 20 (c) Ha=30 (d) Ha=50.*

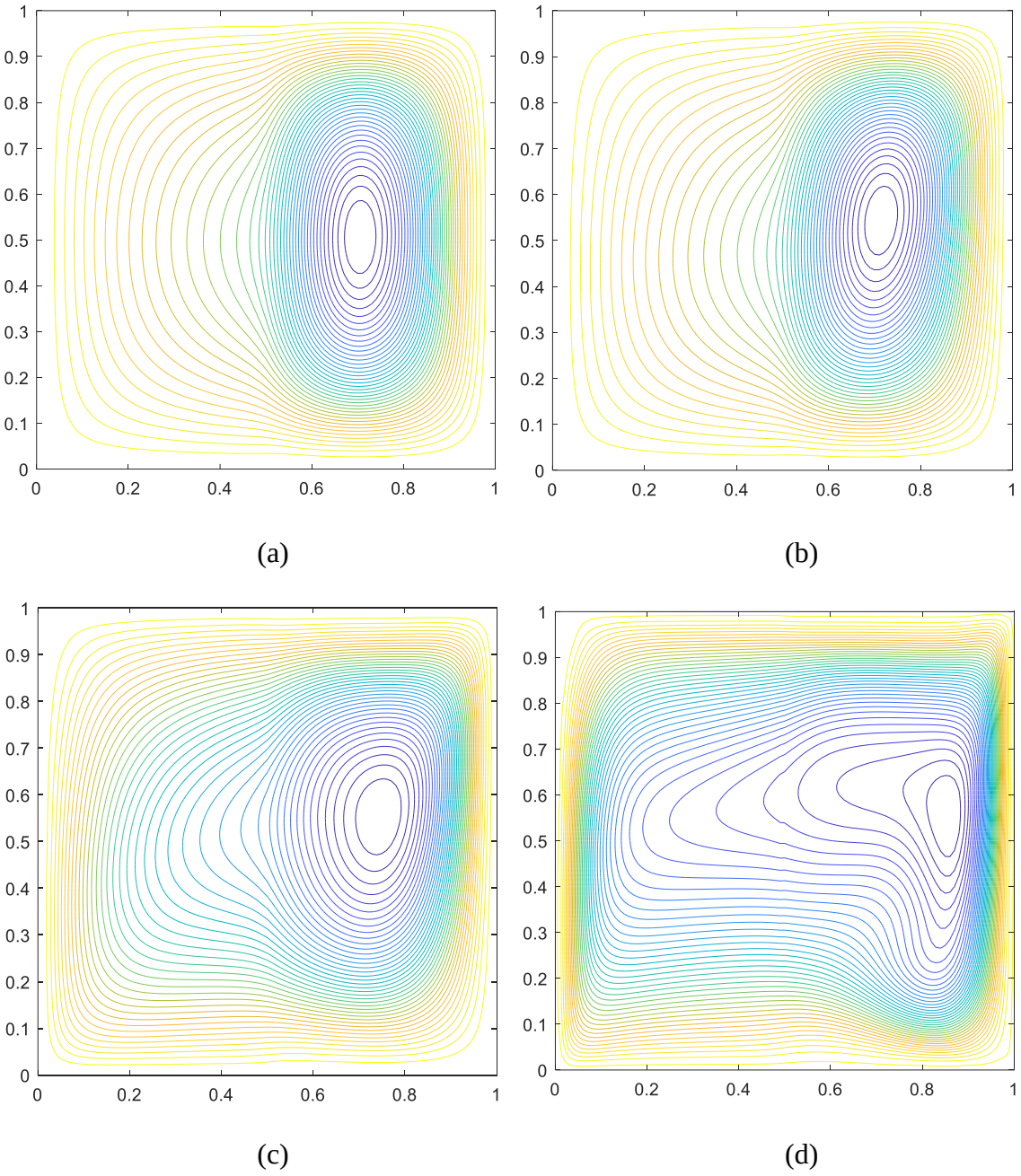

Fig. 10. The influence of Rayleigh number (*Ra*) on streamlines for Da = 0.001, Ha = 5.0: (a) *Ra* = 10^3 (b) *Ra* = 10^4 (c) *Ra* = 10^5 (d) *Ra* = 10^6.

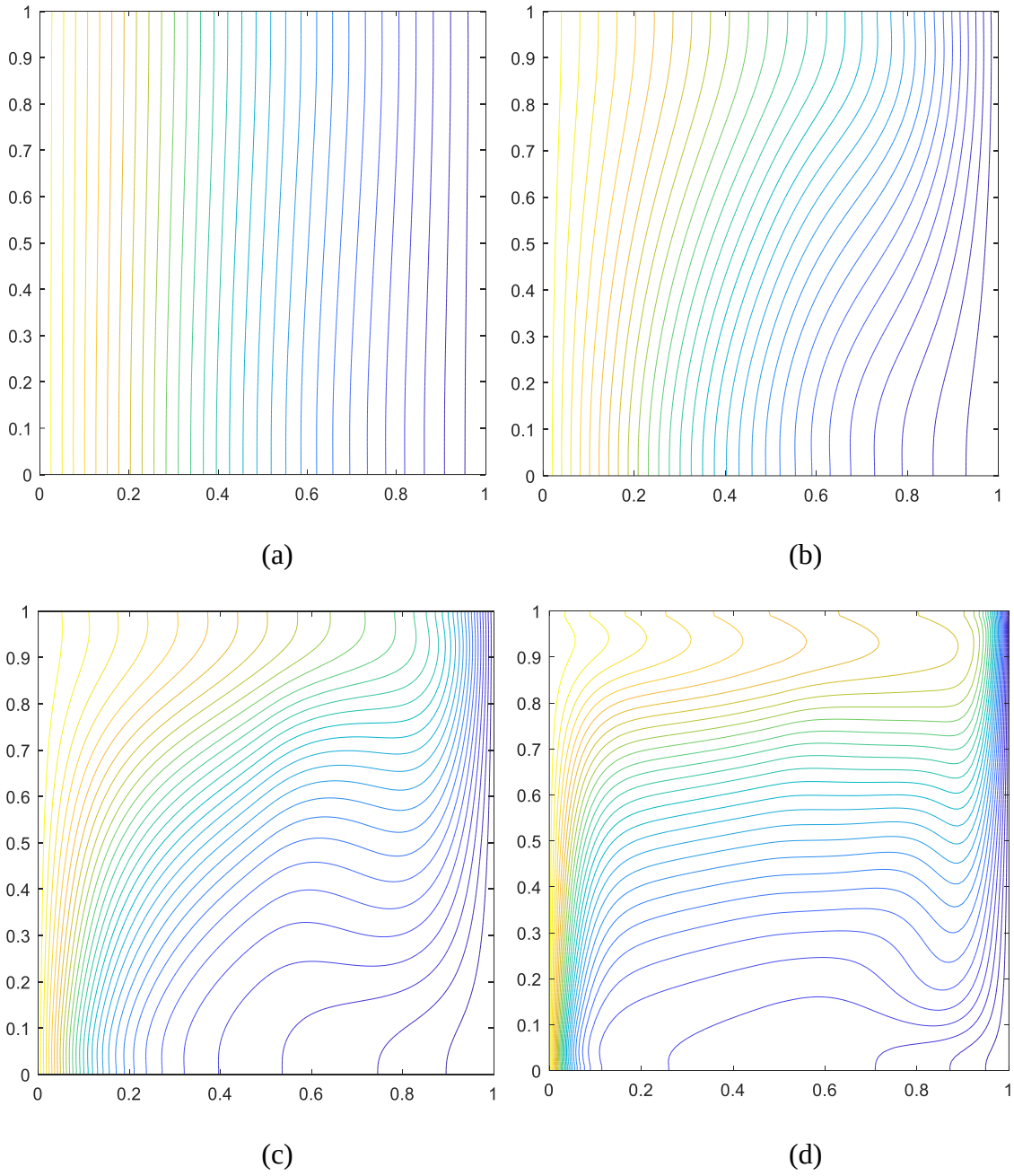

Fig. 11. The influence of Rayleigh number (*Ra*) on isotherms for Da = 0.001, Ha = 5.0: *(a) Ra = 10^3 (b) Ra = 10^4 (c) Ra = 10^5 (d) Ra = 10^6.*

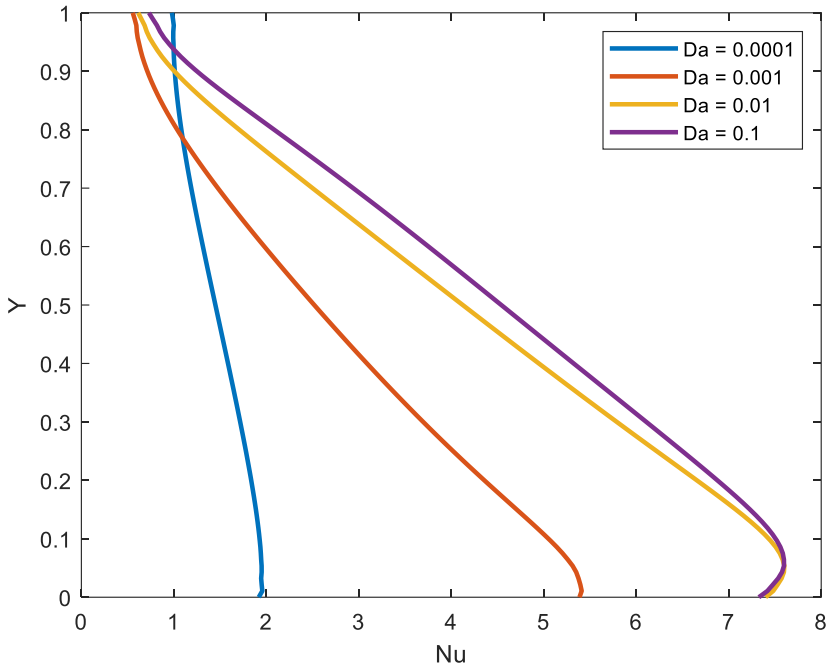

(a)

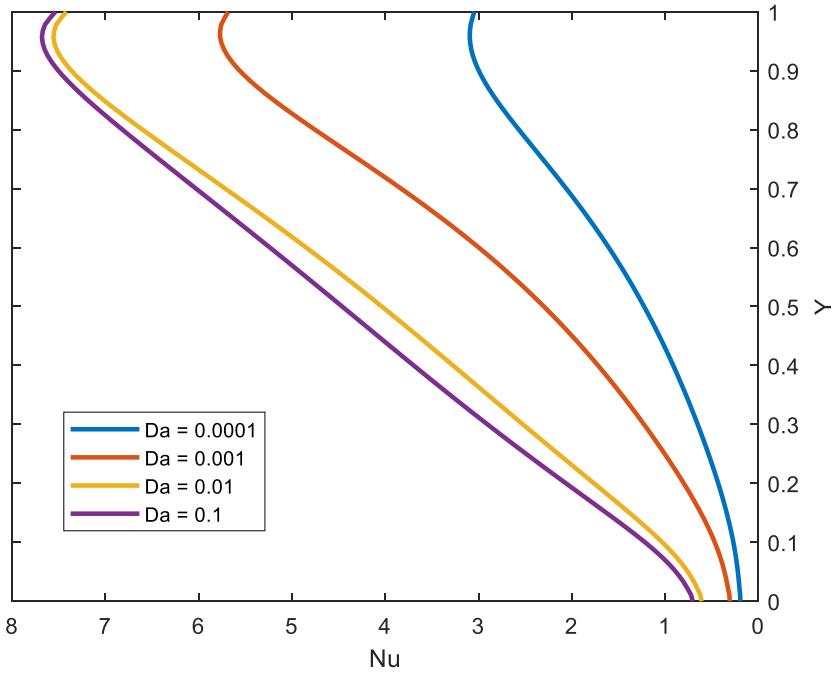

(b)

Fig. 12. Influence of Darcy number (*Da*) on local Nusselt number (heat transfer rate) along the side wall or isothermal wall for *Ha = 5.0 and Ra = 10^5: (a) Left wall (b) Right wall.*

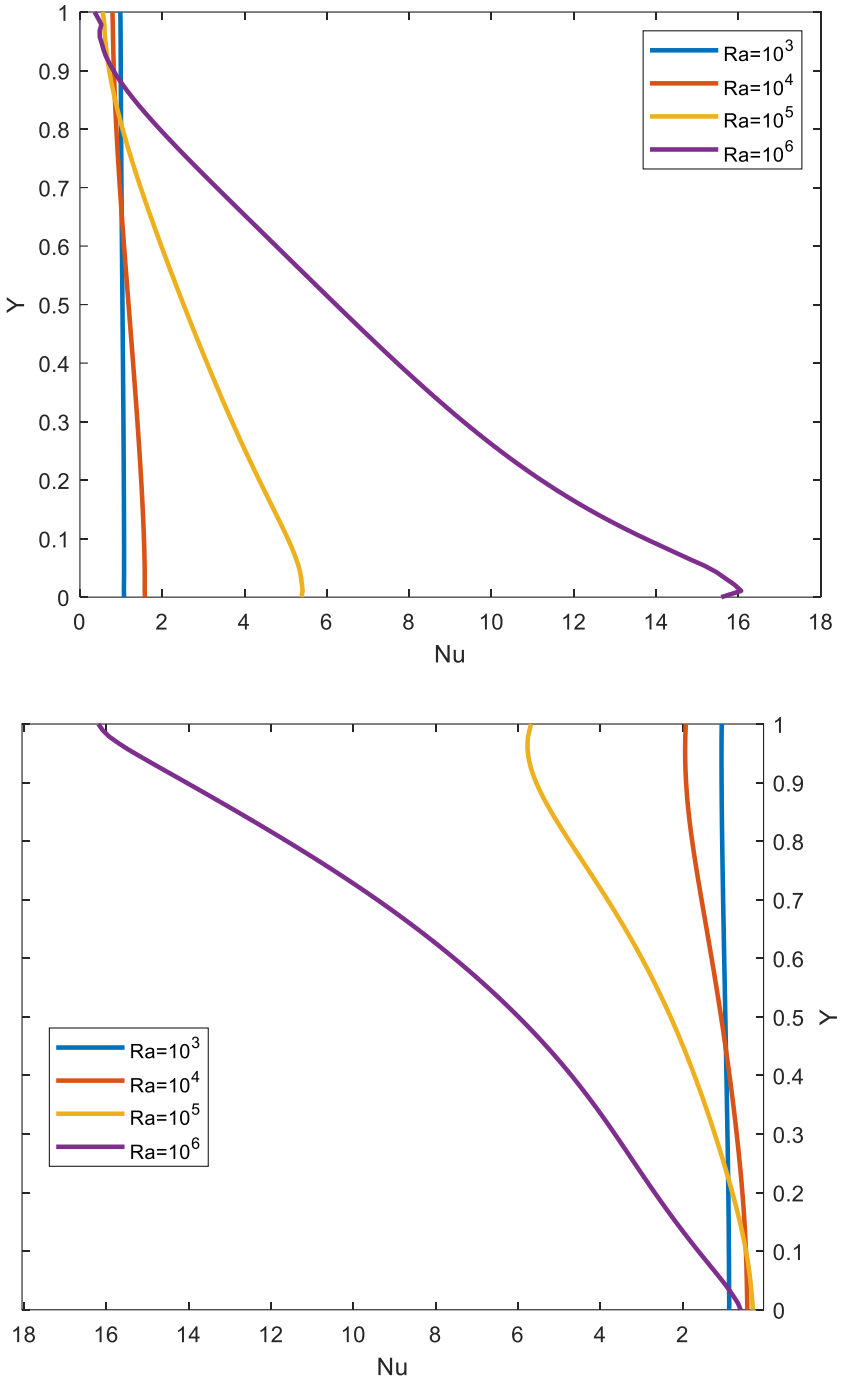

Fig. 13. Influence of Rayleigh number (*Ra*) on Nusselt number (heat transfer rate) along the side wall or isothermal wall for *Da=0.001 and Ha = 5.0*: (a) Left wall (b) Right wall.

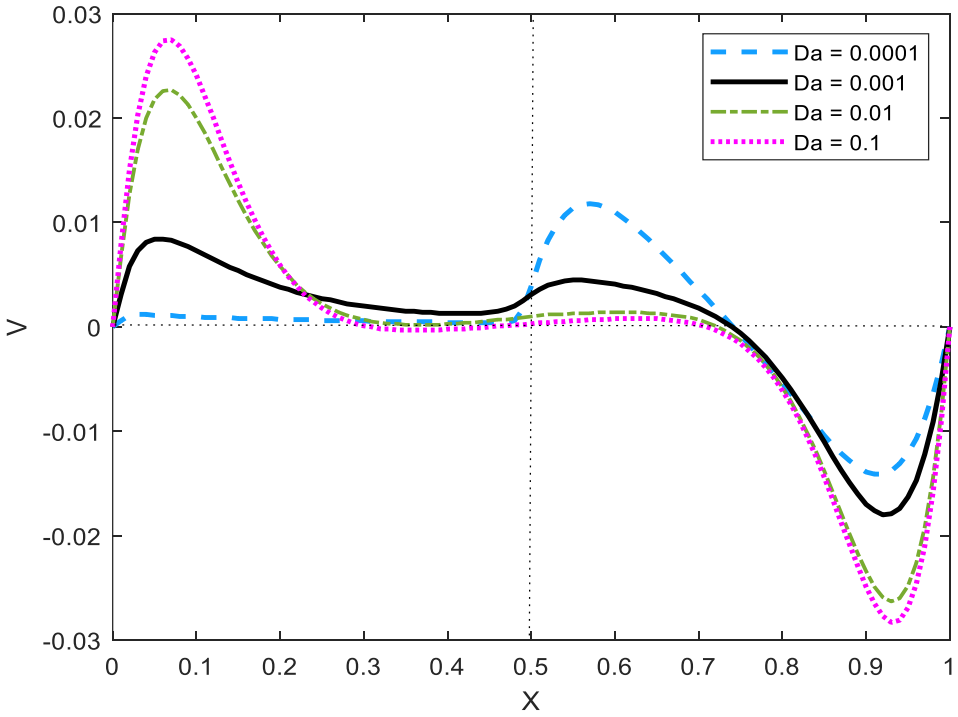

Fig. 14. The influence of the Darcy number on horizontal centre line *secondary velocity profile (V)* for $Ra = 10^5$ *and* $Ha = 5.0$.

6. CONCLUSIONS

As a simulation of emerging magnetized hybrid fuel cell applications, a theoretical analysis of incompressible thermogravitational MHD non-Darcian natural convection in a square enclosure partially filled with a highly permeable porous medium under a transverse magnetic field has been examined by D2Q9-LBM. The percolating fluid considered is electro-conductive Helium gas (Prandtl number (Pr) = 0.71). The present study has shown that:

- As Darcy number increases there is a systematic intrusion of hotter isotherms into the central zone of the enclosure and intensification (heating) further along the upper adiabatic wall and the warmer central zone is expanded.
- Due to symmetry in porous media location, flow patterns are more similar to clear case.
- With greater Darcy number and Rayleigh number, Nusselt number is boosted at the left hot wall and the right cold wall.

- With increasing the flow velocity, the effect of porous media is increased, as a result it can be observed that the effect of porosity and porous part location on flow field increases for higher Rayleigh numbers.
- In low Rayleigh numbers the dominant heat transfer regime is conduction, because the velocity of the fluid is low, the porous media has fewer effect on heat transfer.
- The flow intensification and heat transfer rates are diminishing with increasing of Lorenz force (i.e., Ha).
- In the left porous zone, there is initially a strong elevation in center line secondary velocity with increasing Darcy number, although at higher values it is suppressed.

REFERENCES

[1] Gomez, J.R., Garcia, R.F., Catoira, A.D.M., Gomez, M.R., (2013) Magnetocaloric effect: A review of the thermodynamic cycles in magnetic refrigeration. Renewable and sustainable energy reviews, 17, 74-82.

[2] Rahman S., Masdar M.S., Rosli M., Majlan E., Husaini T., Kamarudin S., Daud W., (2016) Overview biohydrogen technologies and application in fuel cell technology. Renewable and sustainable energy reviews, 66,137–162.

[3] Sun T., Zhang, X., Chen, B., Liu, X. (2019) Coordination control strategy for the air management of heavy vehicle fuel cell engine. International journal of Hydrogen Energy.

[4] Hauer, H., (2005) Magneto tomography—a new method for analysing fuel cell performance and quality. Journal of Power Sources, 143, 67-74.

[5] Abdel-Rehim, A. A., (2019) The influence of electromagnetic field on the performance and operation of a PEM fuel cell stack subjected to a relatively low electromagnetic field intensity. Energy Conversion and Management, 198, 111906.

[6] Ming-Yuan Lin, Lih-Wu Hourng, Chan-Wei Kuo., (2012). The effect of magnetic force on hydrogen production efficiency in water electrolysis. International journal of Hydrogen Energy, 37 ,1311-1320.

[7] Matsushima, H., Iida, T., Fukunaka, Y., Bund, A., (2008) PEMFC performance in a magnetic field. Fuel Cells, 08 (1), pp. 33-36.

[8] Okada, T., Wakayama, N., Wang, L., Shingu, H., (2003) The effect of magnetic field on oxygen reduction reaction and its application in polymer electrolyte fuel cells. Electrochim Acta, 48, pp. 531-539.

[9] Qinqin, T., Shaoqi, Z., (2014) Effect of static magnetic field on electricity production and wastewater treatment in microbial fuel cells. Applied Microbiol Biotechnol., 98, p. 9879.

[10] Ruksawong, K., Songprakorp, R. Monyakul, V., David, N.A., Sui, P.C., Djilali, N. (2017) Investigation of PEMFC under static magnetic field: temperature, relative humidity and performance. Journal of Electrochemical Society, 164 (2), pp. F1-F8

[11] Szczes, A., Chibowski, E., Holysz, L., Rafalski, P., (2011) Effects of static magnetic field on water at kinetic condition. Chemical Engineering Process, 50, 124–127.

[12] Zhang, Y.,(2021) Application of porous materials for the flow field in polymer electrolyte membrane fuel cells, Journal of Power Sources, 492, 229664.

[13] Wang, Y., (2009) Porous-media flow fields for polymer electrolyte fuel cells II. Analysis of channel two-phase flow. Journal of Electrochemical Society, 156, pp. B1134-B1141.

[14] Carton, J.G., Olabi, A.G., (2015) Representative model and flow characteristics of open pore cellular foam and potential use in proton exchange membrane fuel cells, international journal of Hydrogen Energy, 40, pp. 5726-5738.

[15] Lefebvre, L.P., Banhart, J., Dunand, D.C., (2008) Porous metals and metallic foams: current status and recent developments. advanced engineering materials ,10, pp. 775-787

[16] Tan, W.C., Saw, L.H., Thiam, H.S., Xuan, J., Cai, Z., Yew, M.C., (2018) Overview of porous media/metal foam application in fuel cells and solar power systems, Renewable and sustainable energy reviews,96 , pp. 181-197,

[17] Senn, S.M. Poulikakos, D., (2004) Polymer electrolyte fuel cells with porous materials as fluid distributors and comparisons with tranditional channeled systems. ASME journal of Heat Transfer, 126, pp. 410-418,

[18] Kaviany, M., (1995) Principles of Heat Transfer in Porous Media, second ed., Springer, New York, USA.

[19] Cramer, K.C., Pai, S.I., (1973) Magnetofluid Dynamics for Engineers and Applied Physicists, MacGraw-Hill, New York, USA.

[20] Krakov, M. S., Nikiforov, I.V., (2005) Thermomagnetic convection in a porous enclosure in the presence of outer uniform magnetic field. Journal of Magnetism and Magnetic Materials, 289, 278-280 .

[21] Ahmed, S. E., Raizah, Z. A. S.,(2022) Magnetic mixed convection of a Casson hybrid nanofluid due to split lid driven heat generated porous triangular containers with elliptic obstacles, Journal of Magnetism and Magnetic Materials, 559, 169549.

[22] Anwar Bég, O., Venkatadri, K., Prasad, V.R., Bég, T.A., Leonard, H. J., Gorla, R.S.R., Rajarajeswari, P., (2021) Numerical study of magnetohydrodynamic natural convection in a non-Darcian porous enclosure filled with electrically conducting helium gas, Part C: Journal Mechanical Engineering Science.

[23] Tong, T. W., Subramanian, E., (1986) Natural convection in rectangular enclosures partially filled with a porous medium, International Journal of Heat and Fluid Flow, 7, 3-10 .

[24] Al-Nimr, M. A., Khadrawi, A. F., (2003) Transient free convection fluid flow in domains partially filled with porous media, Transport in Porous Media volume 51, 157–172.

[25] Beckermann, C., Ramadhyani, S., Viskanta, R., (1987) Natural convection flow and heat transfer between a fluid layer and a porous layer inside a rectangular enclosure, Journal of Heat Transfer. 109(2): 363-370.

[26] Mohamad, A. A.,(2019) Lattice Boltzmann Method: Fundamentals and Engineering Applications with Computer Codes, Springer, London.

[27] Taher, M.A., Lee, Y.W., Kim, H.D., (2016) LBM simulation on natural convection flow in a triangular enclosure of greenhouse under winter day conditions, Journal of Engineering Thermophysics, 25, 411–423.

[28] Chaabane, R., Jemni, A., (2019) Lattice Boltzmann approach for Magnetohydrodynamic convective heat transfer, Energy Procedia, 162, 181-190.

[29] Dhiraj, M. B., Patil, V., (2020) Power-law fluid flow in driven enclosures with undulation using MRT-lattice Boltzmann method, Computers & Mathematics with Applications, 79, 100-110.

[30] Rabhi, R., (2017) Influence of magnetohydrodynamic viscous flow on entropy generation within porous micro duct using the Lattice Boltzmann Method, RSC Adv., 7, 30673-30686.

[31] Rong, F.,(2010) A lattice Boltzmann model for axisymmetric thermal flows through porous media, International Journal of Heat and Mass Transfer, 53, 5519-5527.

[32] Chai, Z. Shi, B. Lu, J., Guo, Z.,(2010) Non-Darcy flow in disordered porous media: A lattice Boltzmann study, Computional of Fluids, vol. 39, no. 10, 2069–2077.

[33] Hasert, M., Bernsdorf, J., Roller, S.,(2011) Lattice Boltzmann simulation of non-Darcy flow in porous media, Procedia Computional Science vol. 4, pp. 1048–1057.

[34] Sazali, N., (2020) New perspectives on fuel cell technology: a brief review, Membranes, 10(5), 99.

[35] Tang, J., (2012) Perfluorosulfonate ionomer membranes with improved through-plane proton conductivity fabricated under magnetic field. Journal of Membrane science. 423-424, 267–274.

[36] Chu. F.J., (2021) Effects of magnetic fields on electricity generation in a photosynthetic ceramic microbial fuel cell, International Journal of Hydrogen Energy, 46, 11411-11418.

[37] Li, S.,(2008) Direct carbon conversion in a helium fluidized bed fuel cell, Solid State Ionics, 179, 1549-1552.

[38] Alders, M., Winter Halder, D., Wessling, M., (2017) Helium recovery using membrane processes Separ. Purificational Technology, 189, 433-440.

[39] Beg, O. A., Venkatadri, K., Prasad, V. R., Beg, T. A., Kadir, A., and Leonard, H. J. (2020) Numerical simulation of hydromagnetic Marangoni convection flow in a Darcian porous

semiconductor melt enclosure with buoyancy and heat generation effects. Materials Science and Engineering: B, 261, 114722 (2020).

[40] Vahl Davis, D. de., (1983) Natural convection of air in a square cavity: a benchmark solution, International Journal for Numerical Methods in Fluids, 3, 249-264.

[41] Wan, D. C., Patnaik, B. S. V., and Wei, G. W., (2001) A new benchmark quality solution for the buoyancy-driven cavity by discrete singular convolution, Numerical Heat Transfer: Part B, 40: 199-228.

[42] Hamzah, H.K., Ali, F.H., Hatami, M., (2021). Magnetic nanofluid behavior including an immersed rotating conductive cylinder: finite element analysis. Scientific Reports ,**11**, 4463.

[43] Almensoury, M. F., Hashim, A. S., Hamzah, H. K., & Ali, F. H. (2021) Numerical investigation of natural convection of a non-Newtonian nanofluid in an F-shaped porous cavity. Heat Transfer, 50(3), 2403-2426.

[44] Jabbar, M.Y., Hamzah, H.K., Ali, F.H., (2021) Thermal analysis of nanofluid saturated in inclined porous cavity cooled by rotating active cylinder subjected to convective condition. Journal of Thermal Analysis Calorimetry, **144**, 1299–1323.

[45] Hashim, A., Almensoury, M., Farooq, A. L. İ., Hamzah, H., & Ghalambaz, M. (2020). Multiscale Approach of the Equivalent Thermal Conductivity of Modified Foam-Filled and Non-Filled Hollow Brick and a Brick Wall. Journal of Thermal Engineering, 7(1), 190-203.

[46] Abdulkadhim, A., Hamzah, H. K., Ali, F. H., Yıldız, Ç., Abed, A. M., Abed, E. M., & Arıcı, M. (2021). Effect of heat generation and heat absorption on natural convection of Cu-water nanofluid in a wavy enclosure under magnetic field. International Communications in Heat and Mass Transfer, 120, 105024.

[47] Ali, F. H., Hamzah, H. K., Egab, K., Arıcı, M., & Shahsavar, A. (2020). Non-Newtonian nanofluid natural convection in a U-shaped cavity under magnetic field. International Journal of Mechanical Sciences, 186, 105887.

[48] Ali, F. H., Hamzah, H. K., Hussein, A. K., Jabbar, M. Y., & Talebizadehsardari, P. (2020). MHD mixed convection due to a rotating circular cylinder in a trapezoidal enclosure filled with a nanofluid saturated with a porous media. International Journal of Mechanical Sciences, 181, 105688.

[49] Ali, F.H., Hamzah, H.K., Muzaffar, M., (2020) Natural convection of nano encapsulated phase change suspensions inside a local thermal non-equilibrium porous annulus. Journal Thermal Analysis Calorimetry, **141**, 1801–1816.

[50] Hussein, A.K., Hamzah, H.K., Ali, F.H., (2020) Mixed convection in a trapezoidal enclosure filled with two layers of nanofluid and porous media with a rotating circular cylinder and a sinusoidal bottom wall. Journal Thermal Analysis Calorimetry, **141**, 2061–2079.

[51] Aboud, E. D., Rashid, H. K., Jassim, H. M., Ahmed, S. Y., Khafaji, S. O. W., Hamzah, H. K., & Ali, F. H. (2020). MHD effect on mixed convection of annulus circular enclosure filled with non-Newtonian nanofluid. Heliyon, 6(4), e03773.

[52] Al-Amir, Q.R., Ahmed, S.Y., Hamzah, H.K., (2019) Effects of Prandtl Number on Natural Convection in a Cavity Filled with Silver/Water Nanofluid-Saturated Porous Medium and

Non-Newtonian Fluid Layers Separated by Sinusoidal Vertical Interface. Arabian Journal Science and Engineering **44**, 10339–10354.